# Studies of Perovskite-based Materials in Solid Oxide Fuel Cells: Anode Performance Optimization and Degradation Mechanism of Electrolyte

by

Tong Gao

A thesis submitted in partial fulfillment of the requirements for the degree of

Master of Science

in

Chemical Engineering

Department of Chemical and Materials Engineering

University of Alberta

## ABSTRACT

As an alternative energy generation device with higher efficiency compared to conventional devices, the solid oxide fuel cell (SOFC) has been widely investigated. However, the application of SOFC is seriously limited due to the difficulty of maintaining an effective balance between excellent performance and strong stability in operation.

SOFCs can take advantages of fuel flexibility in their potential to use syngas or methane as the fuels. However, the conventional metallic anode catalyst suffers from carbon deposition problems while the perovskite material exhibits a poor performance when fuelled with light hydrocarbons. Therefore, this thesis focuses on enhancing catalytic performance, thermal stability and chemical stability of perovskite materials in syngas by infiltrating the porous substrate with nano-scaled catalysts such as Cu, $CeO_2$ and Co. The results indicated that pre-infiltrating $CeO_2$ into substrate enhanced the thermal stability of the dispersed metallic catalysts. Moreover, with the increase of the amount of catalysts infiltrated, the triple-phase boundary was enhanced until there was an excess amount of metal infiltration that reduced the active sites. The cell with a $La_{0.3}Sr_{0.2}Ba_{0.1}TiO_{3-\delta}$ (LSBT)/yttria stabilized zirconia (YSZ) anode infiltrated with 10.5 weight percent (wt%) $CeO_2$, and 2 wt% Co exhibited excellent electrochemical stability, with only negligible degradation observed under 24-hours tests in syngas.

The second focus of this thesis is the attempt to study the degradation mechanism of $BaCe_{0.7}Zr_{0.1}Y_{0.2}O_{3-\delta}$ (BCZY) discs. In a novel proton-conducting SOFC,

BCZY is applied as the electrolyte because of its high proton conductivity. However, the mechanic properties and electrochemical properties of the BCZY material degrade severely at room temperature. To better understand the degradation mechanism, a number of characterization methods were used, such as scanning electron microscopy (SEM), X-ray diffraction (XRD), transmission electron microscopy (TEM), energy dispersive X-ray spectroscopy (EDS), X-ray photoelectron spectroscopy (XPS) and thermogravimetric analysis (TGA)-mass spectrometry (MS). The results demonstrated that $H_2O$ played a crucial role in initializing the degradation, and $CO_2$ contributed to the subsequent degradation process which resulted in the formation of $BaCO_3$. Based on this mechanism, solutions for preventing degradation when fabricating and storing BCZY discs can be designed.

**Acknowledgements**

I would give my sincere appreciation to my supervisor, Dr. Jingli Luo for all her support and guidance. The greatest gift I received is her knowledge, encouragement and advice which inspired me during two years of research and will continually to drive me to step forward for the rest of my life.

My deep appreciation also goes to Dr. Ning Yan for his valuable advices and suggestive discussions with me throughout the process of my research and thesis writing. His dedication and broad knowledge inspired and motivated me, making my two years of study an extremely valuable and unforgettable experience. I am grateful to Dr. Shaohua Cui, whose advice and knowledge guided me in my research, and whose inspiration shaped me in my life.

I also wish to thank my colleagues and friends, Yifei Sun, Wei Wang, Guangya Wang, Dr. Xinwen Zhou, Dr. Dahai Xia, Chen Shen, Yashar Behnamian, Dr. Hongqiang Fan and Dr. Lixia Yang for all their support, help and encouragement during my stay at the University of Alberta.

My great appreciation goes to the support of Natural Sciences and Engineering Research Council of Canada (NSCERC) Stragetic Grant for financial support.

In the end, I wish to give my special thanks to my parents, whose unconditional love and support are my source of courage for the future.

**Contents**

**List of Figures**

## List of Symbols

| | |
|---|---|
| A | Area |
| $\alpha$ | Transfer coefficient |
| $C_R^B$ | Bulk concentration |
| $C_R^i$ | Interface concentration |
| D | Diffusivity |
| E | Reversible voltage |
| $E^0$ | Standard reversible voltage |
| F | Faraday's constant |
| $\Delta G$ | Gibbs free energy |
| I | Current |
| j | Current density |
| $j_0$ | Exchange current density |
| L | Bond length |
| l | thickness |
| n | Numbers of electrons transferred in a reaction |
| $\eta_{act}$ | Activation overpotential |
| $\eta_{ohm}$ | Ohmic overpotential |
| $\eta_{conc}$ | Concentration overpotential |
| OCV | Open circuit voltage |
| p | Partial pressure |
| $p^\theta$ | Standard pressure of the atmosphere |
| r | Ionic radii |
| R | Gas constant |
| $R_{ohm}$ | Ohmic resistance |
| T | Temperature |

| | |
|---|---|
| t | Tolerance factor |
| V | Voltage output |
| W | Electrical work |
| $\delta$ | Thickness of the diffusion layer |

## List of Abbreviations

| | |
|---|---|
| AFC | Alkaline fuel cell |
| BE | Backscattered electrons |
| BCY | $BaCe_{0.8}Y_{0.2}O_{3-\delta}$ |
| BCZY | $BaCe_{0.7}Zr_{0.1}Y_{0.2}O_{3-\delta}$ |
| BZY | $BaZr_{0.8}Y_{0.2}O_{3-\delta}$ |
| DTA | Differential thermal analysis |
| EDS | Energy dispersive X-ray spectrometer |
| EIS | Electrochemical impedance spectroscopy/spectrum/spectra |
| FT-IR | Fourier Transform Infrared Spectroscope |
| I-V | Current-Voltage curve |
| LSM | $La_{0.3}Sr_{0.2}MnO_{3-\delta}$ |
| LSBT | $La_{0.3}Sr_{0.2}Ba_{0.1}TiO_{3-\delta}$ |
| LST | Lanthanum doped strontium titanate |
| MCFC | Molten carbonate fuel cell |
| MS | Mass spectrometer |
| OCV | Open circuit voltage |
| PAFC | Phosphoric acid fuel cell |
| PEFC | Proton exchange membrane fuel cell |
| SAED | Selected area electron diffraction |
| SE | Secondary electrons |
| SEM | Scanning electron microscope |
| SOFC | Solid oxide fuel cell |
| STEM | Scanning transmission electron microscopy |
| TEM | Transmission electron microscopy |
| TGA | Thermogravimetric analysis |
| TPB | Triple-phase boundary |
| XPS | X-ray photoelectron spectroscopy |
| XRD | X-ray diffraction |

| | |
|---|---|
| YSZ | Yttria stabilized zirconia |

# Chapter 1 Introduction

## 1.1 Energy Generation and Fossil Resource Consumption

Economic development is largely dependent on the consumption of energy. During the past 100 years, the quality of life has significantly improved along with the revolution in energy generation methods [1, 2]. As the most feasible device for generating power, the internal combustion engine was widely applied during the past century. However, the energy generation process of this engine exhausts the world's fossil fuel resources such as coal and oil more rapidly than we wish it to, and causes environmental problems, such as air and water pollutions. The Energy Information Administration assumed that in 2030, fossil fuels including oil, coal and gas would remain the dominant sources of energy, accounting for more than 90% of $CO_2$ production [3, 4]. To reduce the fossil fuel demand and protect our environment, an energy conversion process that is more efficient while emitting fewer pollutants is required.

Alternative methods to generate power are required to meet the strict standards of the 21st century. Novel technologies are required to address concerns that relate to efficiency, pollution management, control of potential hazards [2], economic efficiency and feeds availability [5].

## 1.2 Power Generation from Fuel Cells

Fuel cell is a device that consistently converts chemical energy into electricity. Fuel cells share some characteristics in common with combustion engines and batteries [6]. There are two major benefits of using fuel cells to generate power rather than traditional combustion-based power generation systems: the conversion efficiency is greatly enhanced by directly transforming chemical energy into electrical energy; the emission of pollutants is decreased by the use of an electrochemical

process [1, 2, 6].

In addition, there are also several advantages of using fuel cells as compared to batteries. Batteries need to be charged before functioning, whereas fuel cells can be refueled continuously. Furthermore, a scaling set-up of fuel cells is relatively simple and flexible in comparison with that of the batteries since it has been reported that a megawatt fuel cell stack can be scaled up from single cells with less than 100 W power output [5, 6].

However, fuel cells also possess some disadvantages: despite some limited applications, fuel cells are not economically competitive compared to combustion engines; the power density that illustrates the power produced per unit is not sufficient to meet the requirements of power output as a modern power generation device; the hydrocarbon-fueled cells that take advantage of intrinsic fuel flexibility are still in the research stage due to their poor operational stability [6].

## 1.3 Fuel Cell

### 1.3.1 Components of Fuel Cells

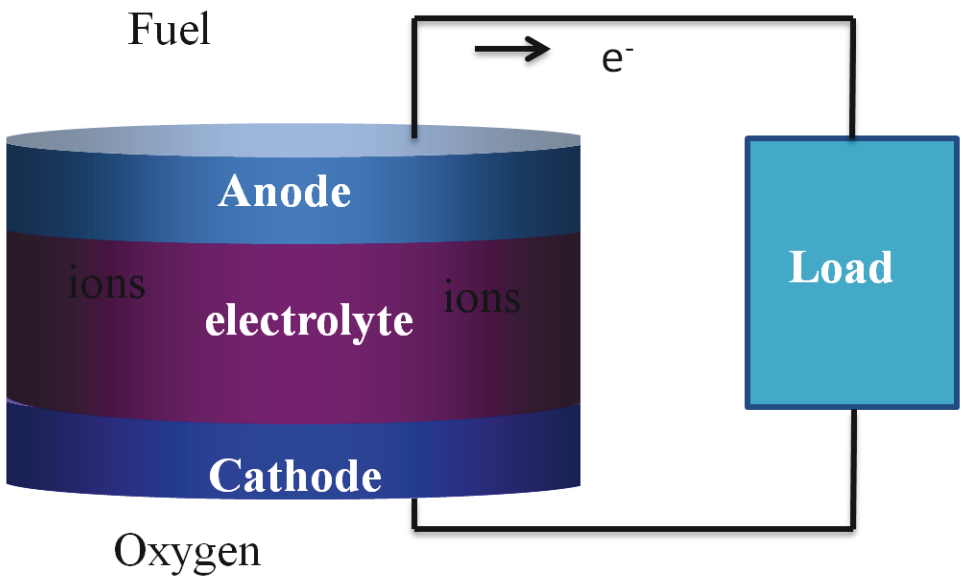


Fig. 1.1. Schematic of fuel cell components.

Fig. 1.1 illustrates the components of a fuel cell. The electrochemical process can be explained in the following steps: Fuels are fed continuously to the anode side where they are activated or ionized. Oxygen or other oxidants are fed continuously to the cathode side where they are activated or ionized. In between, the gas tight electrolyte conducts ions to move from one side to the other in an intrinsic driven circuit that draws electrons to move from the anode to the cathode through an external circuit. As a consequence, electricity is produced as long as inputs are supplied [6].

### 1.3.2 Nernst Equation and Reversible Voltage

The electrochemical reaction that occurs in fuel cells can be represented through the fundamental rules of thermodynamics in terms of power output and maximum voltage.

For fuel cells, the maximum electrical work (W), generated from a reaction, equals to the Gibbs free energy ($-\Delta G$), as shown below:

$$E = \frac{W}{nF} = \frac{-\Delta G}{nF} \tag{1.1}$$

where E is the reversible voltage, n is the number of electrons transferred in a reaction, and F is the Faraday's constant.

The maximum voltage in fuel cells, E, can be calculated by the Nernst equation.

For conventional $H_2$-fueled cells, the reactions on both sides are written as follows:

$$\text{Cathode: } \frac{1}{2}O_2 + 2e^- = O^{2-} \tag{1.2}$$

$$\text{Anode: } O^{2-} + H_2 = H_2O + 2e^- \tag{1.3}$$

$$\text{Total: } \frac{1}{2}O_2 + H_2 = H_2O \tag{1.4}$$

The reversible voltage E can be calculated by the following:

$$E = \frac{-\Delta G}{2F} = E^0 + \frac{RT}{2F} \ln \frac{(p_{O_2})^{0.5} p_{H_2}}{p_{H_2O}} \quad (1.5)$$

$p_{O_2}$, $p_{H_2}$ and $p_{H_2O}$ are the partial pressures of oxygen, hydrogen and stream, respectively, $E^0$ is the standard reversible voltage.

### 1.3.3 Polarizations

The performance of fuel cells is determined by their polarizations, which can be categorized into activation polarization, ohmic polarization and concentration polarization. The current density-voltage (j-V) curve, which is usually represented by current density-voltage, represents different stages of the polarization process (Fig. 1.2).

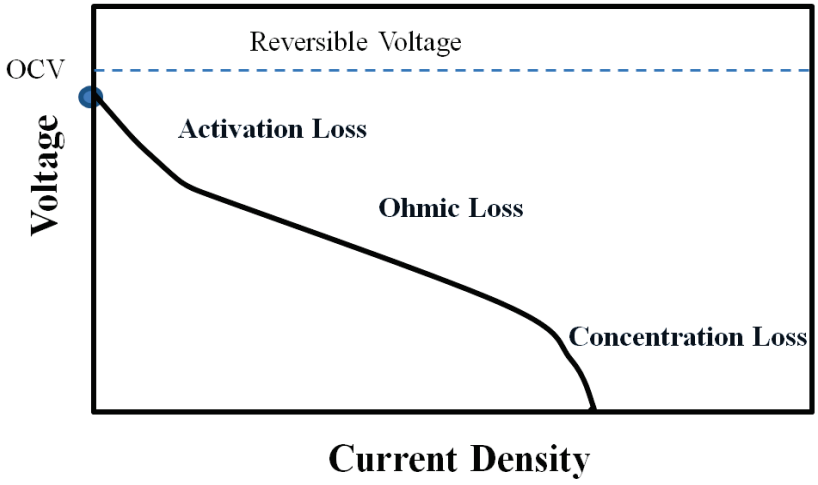


Fig. 1.2. Schematic of current density-voltage curve for fuel cells.

The measured open circuit voltage (OCV) is lower than the reversible voltage due to the crossover of fuels and internal electrical short circuiting caused by the small electronic conductivity of the electrolyte. The voltage output (V) is the OCV minus activation overpotential ($\eta_{act}$), ohmic overpotential ($\eta_{ohm}$) and concentration overpotential ($\eta_{conc}$), which correspond to different polarization processes.

$$V = OCV - \eta_{act} - \eta_{ohm} - \eta_{conc} \quad (1.6)$$

1.3.3.1 Activation Overpotential

The relationship between current density (j) and $\eta_{act}$ ) is described by the Butler-Volmer equation:

$$j = j_0 \left\{ \exp\left[\frac{\alpha\, nF\eta_{act}}{RT}\right] - \exp\left[\frac{-(1-\alpha)nF\eta_{act}}{RT}\right] \right\} \quad (1.7)$$

where R is the universal gas constant , $\alpha$ is the transfer coefficient, $j_0$ is the exchange current density where the forward current density equals the backward current density, and T is the absolute temperature. The equation describes a reaction occurring at the interface between the electronic and the ionic conductors.

1.3.3.2 Ohmic Overpotential

At the middle range of the j-V curve, the potential loss is dominated by ohmic polarization. The ohmic polarization results from the ohmic resistance $R_{ohm}$ of the anode, cathode, and electrolyte and the contact resistance $R_{contact}$. The relationship between ohmic overpotential $\eta_{ohm}$ and current I can be described in the equation below:

$$\eta_{ohm} = I(R_{ohm(anode)} + R_{ohm(cathode)} + R_{ohm(electrolyte)} + R_{contact}) \quad (1.8)$$

The ohmic resistance of each component can be calculated by

$$R_{ohm} = \rho\frac{l}{A} \quad (1.9)$$

The resistance is a function of the intrinsic resistivity ρ, the area A and the thickness l. Since the electrical conductivities of electrodes are much higher than the electrical conductivity of the electrolyte, the main contributor of ohmic resistance is

usually low conductivity of thick electrolytes. Approaches have been made to produce thinner electrolytes and to find electrolyte materials with lower intrinsic ionic resistivity.

1.3.3.3 Concentration Overpotential

Mass transfer limitation controls the electrochemical process at a high current density. The limitation results from the diffusion of reactants and products through the gas channels. The diffusion process can be described by Fick's law that indicates the concentration change of reactants at the interface and at the bulk.

$$C_R^B = C_R^i + \frac{j\delta}{nDF} \tag{1.10}$$

In the equation 1.12, $C_R^B$ is the bulk concentration, $C_R^i$ is the concentration at the interface, D is the diffusivity and $\delta$ is the thickness of the diffusion layer.

The mass transfer overpotential is caused by the concentration difference:

$$\eta_{conc} = -B\ln\left(1 - \frac{j}{j(C_R^i=0)}\right) \tag{1.11}$$

where B is an empirically predicted constant.

### 1.3.4 Classification of Fuel Cells by the Electrolytes

There are several types of electrolytes by which fuel cell are classified, shown in Fig. 1.3 [6].

Proton exchange membrane fuel cells (PEFCs) use polymer membranes that conduct $H^+$ from the anode to the cathode. For this reason, $H_2$ is considered as the only proper fuel for PEFC and the operating temperature is lower than 100 $^oC$.

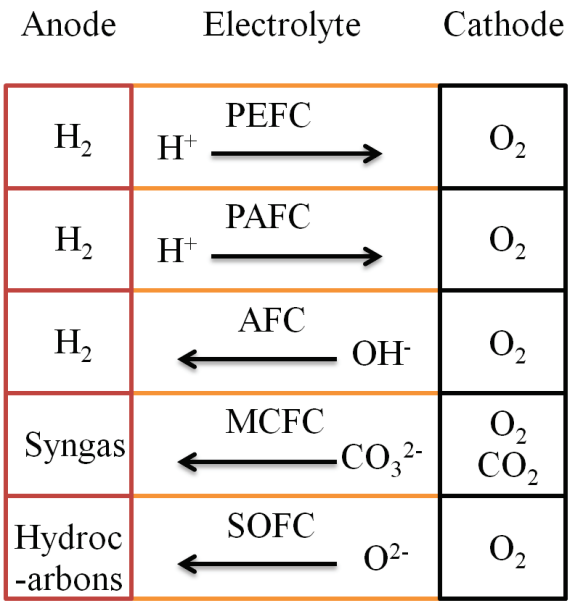


Fig. 1.3. Classification of fuel cells,

The electrolytes of phosphoric acid fuel cells (PAFCs) work in concentrated phosphoric acid, which also conduct $H^+$ from the anode to the cathode. Both $H_2$ and syngas are used as fuels, and the operating temperature is set at around 200 $^oC$ to increase the ionic conductivity and to avoid carbon deposition.

The electrolytes of alkaline fuel cells (AFCs) conduct $OH^-$ ions from the cathode to the anode. The electrolytes are made of an alkaline solution that is infiltrated in a matrix of asbestos support. The fuel is limited to hydrogen to eliminate side reactions, and the operating temperature is usually determined by the concentration of the solution.

The electrolytes of molten carbonate fuel cells (MCFCs) conduct $CO_3^{2-}$ from the cathode to the anode. The operating temperature is over 600 $^oC$ to reduce the carbon deposition on the anode when operating in syngas. The fuel cell needs a recovery process to maintain the conductivity of the electrolyte, which is composed of a molten carbonate salt mixture suspended in a porous ceramic matrix of beta-alumina.

Traditional solid oxide fuel cells (SOFCs) employ ceramics that conducts $O^{2-}$ from the cathode to the anode as the electrolyte. Recently, a proton conducting SOFC has been investigated, in which $H_2$ is ionized at anode to form protons that transfer

from the anode to the cathode.

## 1.4 Solid Oxide Fuel Cells

### 1.4.1 Principle of SOFCs

The major benefits of SOFCs are the superior fuel flexibility and the high efficiency. Compared with other types of fuel cells, SOFCs enable the conversion of various hydrocarbons since they operate at a wider range of high temperatures, from 650 $^{o}$C to 1000 $^{o}$C. Moreover, the waste heat exhausted can be recycled according to the system design. In addition, SOFCs are relatively insensitive to impurities, which suggests the possibility of the utilization of "hazard or worthless gases" such as $H_2S$ as well as light hydrocarbons as the fuels [6, 7]. These properties largely depend on the high operating temperature which brings challenges for using SOFCs.

SOFCs were firstly investigated in 1937. A zirconia tube was used as the electrolyte with carbon/iron applied as anode and magnetic ferric oxide as the cathode. The primary limitation was the performance of electrolyte until yttrium stabilized zirconia (YSZ) found by Nernst was introduced as a stable electrolyte material. It was explained that the ionic conductivity was actually based on the oxygen vacancy mobility [5, 6]. The finding established the foundation of SOFCs for which 8 % yttrium-doped zirconia was finally recognized as the proper $O^{2-}$ conducting electrolyte.

The operating temperature is one of the most important parameters that determine the designs and developments of SOFC component materials. Although the higher operating temperature reduces the activation loss of electrode(s) and enables effective conversion of a wide spectrum of light hydrocarbon fuels in fuel cells, a lower operating temperature permits the use of cost-effective materials, e.g., metallic interconnects, and reduces the thermal stress during fuel cell startup-shutdown cycles [6]. Since the adequate conductivity for ion transfer in YSZ depends on an operating temperature that is usually above 800 $^{o}$C [5, 6], YSZ is widely applied on high temperature operating SOFCs. Novel electrolyte materials have been investigated to

apply high efficiency catalysts on intermediate temperature fuel cells that offer obvious economic benefits.

### 1.4.2 Triple-Phase Boundary (TPB)

The current density generated from the electrochemical process is a strong function of the performance of the catalyst and efficient catalytic area, so the design of the electrode focuses on optimizing these two parameters. An efficient ionization process in a conventional SOFC requires the catalytic activity to initialize the reactions, the ionic conductivity to provide oxidants and the electrical conductivity to collect and transfer electrons so as to complete the external circuit. These three properties are critical because insufficiency of any of these properties would result in poor performance of the electrode, i.e., the poor performance of the fuel cell.

On top of the material properties, a porous substrate is demanded in terms of gaseous diffusion. A highly porous nano-structured electrode which provides intimate contact between the gas, electrode and electrolyte is always preferred to maximize the number of reaction sites. The reaction site is called the triple-phase boundary or TPB in fuel cells where reactions can only occur as shown in Fig. 1.4 [5, 6, 9].

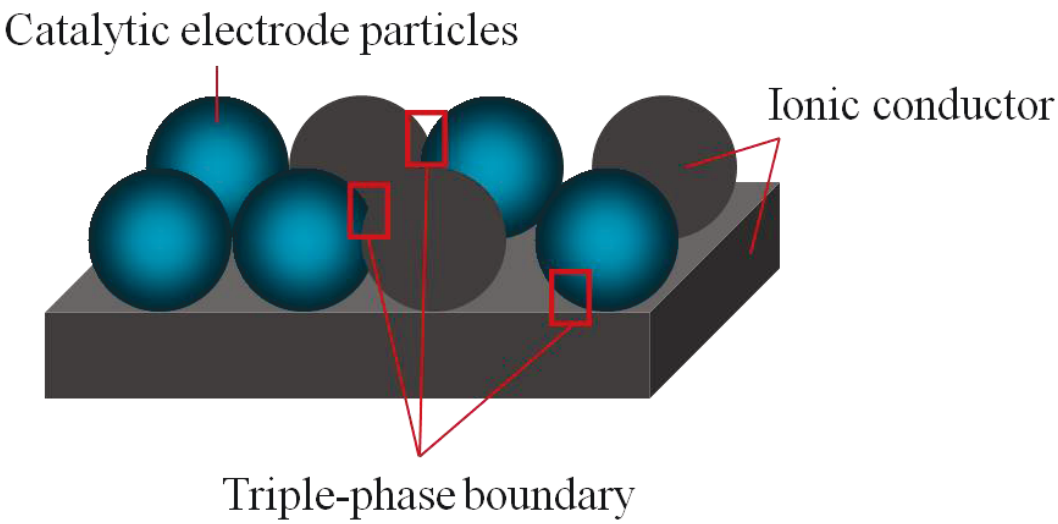


Fig. 1.4. Schematic of TPB of electrode in SOFCs.

### 1.4.3 Cathode

The cathode drives the reduction of oxygen. There are several basic requirements for reducing $O_2$ efficiently: high catalytic activity, sufficient electronic and ionic conductivities, adequate compatibility with other components and excellent porosity for gas diffusion at the interface at operating temperatures. Originally, Pt was applied as the cathode catalyst for SOFCs. However, the cost of the precious metal made it unfavorable for commercialization. A series of promising alternatives to using Pt as the cathode catalyst is found in perovskite-based materials, presently considered as the most suitable class of materials for SOFC cathode applications. Strontium-doped lanthanum manganite (LSM) [10] is one of the most widely used cathode materials and provides reasonable catalytic activity for reducing oxygen and conducting electron.

### 1.4.4 Anode

Electrochemical oxidation of fuel occurs on the anode. To achieve an efficient fuel conversion, a candidate anode catalyst is required to exhibit high catalytic activity, adequate electronic and ionic conductivities, excellent chemical and mechanical compatibilities with the electrolyte and interconnects, sufficient porosity for gas diffusion at the interface, and good resistivity against carbon formation.

### 1.4.5 Development of Anode Catalysts

#### 1.4.5.1 Current Anode Limitations of SOFCs

The traditional anode for SOFCs, Ni/YSZ cement, provides excellent electrochemical performances. In the cement, YSZ provides excellent structural support and $O^{2-}$ conductivity while Ni acts as the anode catalyst and the electronic conductor. However, a Ni/YSZ anode has several limitations:

①The strong tendency to catalyze the formation of carbon can produce carbon filaments that tend to expand and lead to catastrophic fracture of Ni [11].

② The poor wettability of YSZ by nickel results in agglomeration of Ni metal, while the micro-structural change causes degradation of the catalyst [12].

Among all these drawbacks, a major concern associated with the stability is the carbon deposition, which involves the formation of graphite on the metallic surface and the dissolution of the carbon fiber into the lattice of Ni crystalline [13, 14]. As a result, metal dusting causes structured disintegration of Ni.

Efforts have been devoted to suppress carbon formation at the surface by introducing humid fuels to the anode. However, high ratio of $H_2O$ to C was required to suppress carbon deposition at the expense of reduced efficiency of fuel cells [14].

#### 1.4.5.2 Alternative Candidates for the Anode

To increase the stability of anode catalysts, Ni was replaced with other materials. The novel anode catalysts can be categorized into two major groups: ceramic-metal composites and complex oxides.

##### 1.4.5.2.1 Ceramic-Metal Composite Catalyst

Metallic catalysts have been incorporated on the surface of ceramic substrate that provides mechanic support and ionic conductivity. Replacing Ni with a kind of metal that does not catalyze the formation of carbon has proven to be feasible [15, 16, 17]. Compared to Ni, neither Cu nor Au catalyzes the cracking of hydrocarbons [15, 16]. Although the process of gas-phase pyrolysis is unavoidable, the deposited carbon does not destroy the structure of metallic anode catalysts. Ceria, which demonstrated a good balance between catalytic activity and chemical stability in hydrocarbons, has been shown to be a proper catalytic material for the anode. As an infiltrate into the anode substrate, it also optimized the microstructure of the anode and increased the stability of metallic catalysts [17]. In the category of precious metals, well dispersed Rh, Pd and Ru particles are also good candidate materials that exhibit high catalytic activity and electrical conductivity. However, the thermal stability they exhibited was relatively poor at temperature around 850 $^{o}$C [18].

Composite catalysts that provide a good balance between catalyzation and

stability were well investigated. Cu-ceria [19] and Pd-ceria [20] were studied to directly utilize hydrocarbons. Cu was believed to provide electronic conductivity, whereas ceria provided catalytic activity and mixed conductivity. The Cu-ceira cell exhibited a reasonable performance and sulfur tolerance, however, the fabrication method of the Cu-ceria electrode was relatively complicated due to the low melting point of Cu, which resulted in a loss of electronic conductivity and power output. In the Pd-ceria cell, Pd provided catalytic activity while ceria enhanced thermal stability of Pd. This cell exhibited an excellent performance and a reduced rate of degradation in the long-term stability test.

1.4.5.2.2 Oxide Catalysts

Mixed ionic and electronic conductors compound with high resistivity towards carbon deposition and sulfur poisoning, is another alternative for Ni as the anode catalyst for SOFC. Among the oxide catalysts, perovskites are the most widely applied material as anode catalysts, which will be discussed in Section 1.5.

1.4.5.3 Infiltration Method

A strategy for achieving an excellent performance is to combine the two types of materials by introducing an active metallic catalyst into the perovskite-based anode.

The fabrication of electrodes for SOFCs by infiltrating metallic catalysts into a sintered porous perovskite-based skeleton holds significant potential for the development of anodes. When compared with conventional solid state synthesis, the wet infiltration method is a low cost and highly efficient process. Additionally, the uniformly dispersed infiltrates over the substrate materials surface are beneficial in maintaining a high redox and chemical stability in hydrocarbons. The impregnation method for electrode fabrication involves infiltrating the porous electrode matrix with corresponding metal nitrates aqueous solutions. The cell is then dehydrated and heated to decompose the nitrates and form oxides at a relative low temperature to restrain the particle sizes of catalysts. Upon reduction, the oxides will be transformed into finely structured nano-scaled metallic catalysts, which greatly enhance the TPB

in fuel cell operation.

## 1.5 Applications of Perovskite Materials in SOFCs

### 1.5.1 Perovskite Structure

The $ABO_3$ perovskite encompasses a variety of different compounds. Generally, the large cation A comes from alkali, alkaline earth or rare earth metals in the periodic table, while small cation B comes from transition metal ion. A three-dimensional framework of $BO_6$ octahedra characterizes the crystal structure of perovskite. As shown in Fig. 1.5, each B atom is at the center of an octahedron, with six O atoms surrounding it and connected to one another. Each A atom is arranged in a site surrounded by eight octahedrons. In the ideal cubic structure, the bond lengths of B-O and A-O have the following relationship:

$$L_{A\text{-}O} = \sqrt{2}\, L_{B\text{-}O} \tag{1.12}$$

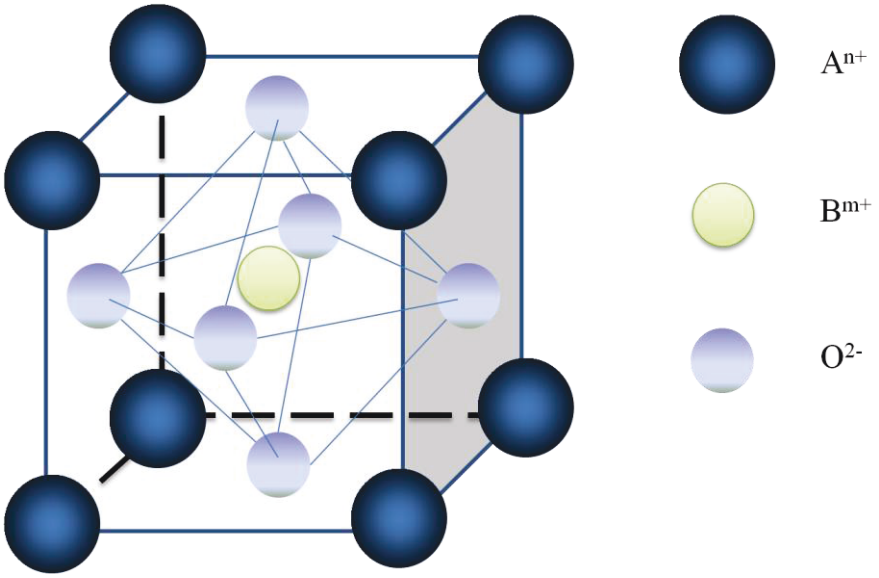


Fig. 1.5. The ideal perovskite structure with a B atom at the body center.

However, the relative sizes of cation A and cation B are not matched exactly. The structure of the octahedron rotates or tilts to fit the mismatch, which eventually distorts the structure. This distortion is described by a tolerance factor of t, in the

equation 1.13:

$$t = \frac{r_A + r_o}{\sqrt{2}(r_B + r_O)} \quad (1.13)$$

where $r_A$, $r_O$ and $r_B$ are the ionic radii of A, O and B, respectively. The structure is cubic when t is close to 1, transforms to rhombohedral when t is between 1 and 0.96, and transforms to an orthorhombic structure when t is smaller than 0.96.

### 1.5.2 Performance of Perovskites

The distortion effect characteristic of the perovskite structure can be reduced with the presence of oxygen vacancies. The perovskite oxide has a relatively stable structure capable of hosting the multiple dopants of A and/or B site occupation, with a charge balance maintained by formation of holes or charged oxygen vacancies [22]. Aside from reducing the distortion, the perovskite compounds exhibit a variety of unique physical properties, especially ionic and electronic conductivities, which play an important role in the electrochemical performance of SOFCs. The perovskites typically used in SOFCs is introduced as below.

Perovskite structures have been widely studied in terms of ionic and electronic conductivity at high temperature in a reducing atmosphere. A perovskite structure with the stoichiometry of $ABO_3$ provides alternatives to Ni/YSZ as catalysts for carbon and sulfur resistant anodes [23], alternatives to Pt as catalysts for the cathodes [24] and, as proton conducting materials for the electrolytes [25].

#### 1.5.2.1 Barium Cerate-Zirconate

In the early 1980's, Iwahara proved that a number of II-IV perovskites demonstrated proton-conducting capability, when the A cation comes from alkaline earth metal and the B cation comes from Group 4 of the periodic table [26, 27]. Since then, more perovskites with proton conductive characters have been investigated.

The mechanism of proton conduction starts with the formation of protonic

defects when water or hydrogen from the gas phase dissociates. With the hydroxide ion filling into the oxygen vacancy of the material, the proton forms a covalent bond with the oxygen that transfers through the lattice.

However, the solubility of proton into traditional perovskites brings about an unfavorable introduction of charged defects into the electroneutral material. To maintain the oxygen vacancy, trivalent dopants were introduced with tetravalent cations [26, 27].

Barium cerate exhibits enhanced protonic conduction in moist atmospheres when it received a partial substitution of trivalent dopant cation [28, 29, 30]. The $BaCeO_3$ and $BaZrO_3$ system, with various dopants such as Y and In, has been widely investigated for providing the electrolytes [28, 29] of proton-conducting SOFCs. In 1993, Iwahara [31] synthesized $BaZrO_3$ with Y doped into the B site. With a low concentration of Y, the structure of $BaCeO_3$ transforms from an orthorhombic structure into a cubic structure. At room temperature, the doped $BaCeO_3$ exhibits two non-equivalent oxygen sites, while $BaZrO_3$, on the other hand, exhibits a cubic symmetry.

The thermodynamic properties of $BaCeO_3$ were measured and it was shown that $BaCeO_3$ is not stable with even small amounts of $CO_2$, with decomposition reactions shown below [28]:

$$BaCeO_3 + CO_2 = BaCO_3 + CeO_2 \quad (1.14)$$

Additionally, $BaCeO_3$ was also proved to be unstable in wet air with $PH_2O$ at around 430 torr, the decomposition reactions is shown below:

$$BaCeO_3 + H_2O = CeO + Ba(OH)_2 \quad (1.15)$$

The poor stability of $BaCeO_3$ intensively limits its application in SOFCs application since the formation of water is inevitable.

Doping $Zr^{4+}$ to partially substitute $Ce^{4+}$ on the B site increases the chemical

stability of the material [29, 30, 31]. However, the conductivity of the material was, therefore, reduced.

1.5.2.2 Strontium Titanate

Among the three major series of perovskite anode catalysts, chromate, titanate and vanadate, $SrTiO_3$ received the greater interests in potential application as anode catalysts [32].

The mechanism of the mixed electronic and ionic conductor $SrTiO_3$ is that in a reducing atmosphere, the formation of oxygen vacancy leads to the increase in ionic conductivity with the coherent reduction of $Ti^{4+}$ to $Ti^{3+}$, therefore, $SrTiO_3$ is an n-type semiconductor, [6, 23].

Donor doping of the A site affects the properties of the perovskite structure by weakening the Ti-O bond. Electrical conductivity and ionic conductivity can be increased by doping A site with La, and Y, while ionic conductivity and catalytic activity can be increased by doping the B site with Ni, Co, etc [23, 26]. For instance, the $La_{0.3}Sr_{0.2}Ba_{0.1}TiO_3$ (LSBT) anode catalyst was investigated with La dopant to enhance the electrical conductivity and Ba dopant to enhance the ionic conductivity and stability in hydrocarbons [32]. $La_{0.2}Sr_{0.8}Co_xTi_{1-x}O_3$ was investigated with La dopant to enhance the electrical conductivity and Co dopant to enhance the catalytic activity, as well as the stability of the material.

Although the doped $SrTiO_3$ materials provide high electronic conductivity, they are not comparable to metallic anode. Unlike chromites [33], Ti tends to keep its octahedral structure, which results in low ionic and electrical conductivities. Moreover, the catalytic activity of perovskite is not comparable to that of metallic anode catalysts, such as Co and Ni.

## 1.6 Summary

The achievements in the development of SOFCs are reviewed in chapter 1. SOFCs are designed as electrochemical reactors in which both CO and $H_2$ can be

oxidized at the anode. In the oxygen conducting SOFCs, where yttria-stabilized zirconium works as electrolytes, conventional Ni/YSZ anode catalysts are limited due to carbon deposition, while the carbon resistant perovskite material as anode catalyst exhibits relatively poor performance. Approaches have been made to balance the excellent performance with high stability by infiltrating metallic catalysts into the perovskite-based substrate.

To enhance the performance of SOFCs at intermediate temperature, researchers turned their attention to the study of proton-conducting SOFCs. As a novel proton-conducting material, $BaCe_{0.7}Zr_{0.1}Y_{0.2}O_{3-\delta}$ (BCZY) has attracted much interest. However, the perovskite structure of the material endures an inevitable degradation in acidic and wet gases.

## 1.7 Objectives and Thesis Contents

This thesis is focused on two objectives: achieving a balance between excellent performance and carbon resistance; and understanding the mechanism of degradation of BCZY.

Chapter 2 describes the methodology, including the synthesis of materials, fuel cell set-up, electrochemical tests and characterization methods.

The objective of Chapter 3 is to prepare LSBT-based material with the impregnation method that is used as the anode of SOFC powered by syngas. The investigation focused on providing a well distributed catalyst on the anode surface which enhanced the catalytic ability of the anode catalyst while maintaining the chemical and structural stability in syngas.

The degradation mechanism of the proton-conducting electrolyte BCZY was investigated in Chapter 4. With the means of characterization methods, the reason for structural transformation was revealed with possible solutions suggested for the design of fabrication and storage system against the degradation of the material.

Conclusions and future work are presented in Chapter 5.

# Chapter 2 Methodology

## 2.1 Fabrication of SOFCs with LSBT-Based Anode

Yttria stabilized zirconia (YSZ) was used as the electrolyte material. The operating temperature was between 850 $^{o}$C and 950 $^{o}$C so that YSZ electrolytes had sufficient conductivity.

LSBT was prepared using the solid state synthesis method. The starting materials were 3.9095 g $La_2O_3$ (Alfa 99.99%), 4.7922 g $TiO_2$ (BDH 98%), 4.4289 g $SrCO_3$ (Fisher 99.0%) and 1.1841 g (± 0.0005 g) $BaCO_3$ (Fisher 99.4%). The powders were ball milled and mixed uniformly. The mixed powders were pressed at 200 Mpa and calcined at 1200 $^{o}$C for 10 hours (± 1 min), ball milled and repressed at low pressure. The pellets were calcined at 1500 $^{o}$C for four hours.

The impregnation solution was prepared by mixing nitrates with deionized water: a cerium nitrate solution was made at a concentration of 4.0 (± 0.5) mol $L^{-1}$; a cobalt-copper nitrate solution was made at a molar ratio of 3:2 at a total metal concentration of 3.0 mol $L^{-1}$; a cobalt-cerium solution was made at a mole ratio of 4:3 at a total metal concentration of 3.0 (± 0.5) mol $L^{-1}$. The co-impregnation was applied to maintain a constant ratio of catalysts which dispersed evenly on the substrate with a consistant performance of infiltrates. 10 wt% of polymer microspheres (Polymethylmethacrylate PMMA Spheromers, CA 6, Microbeads, Skesmokorset, Norway) were mixed with 50 wt% LSBT and 50 wt% YSZ to achieve a high level of porosity in the anode layer. 10 wt% of PMMA was mixed with 50 wt% LSM and 50 wt% YSZ as the cathode material. The two electrode materials were dispersed in fuel cell gel with a-terpineol (Alfa Aesar): isopropanol = 2 : 1 as a solution containing 5 wt% poly(vinyl butyral-co-vinyl alcohol-co-vinyl acetate) (PVB, Mw = 70 000–100000, Aldrich) and 5 wt% ethyl cellulose (Aldrich) to form electrode inks.

The electrolyte was commercial YSZ discs with a thickness of 250 μm to 300 μm. Anode and cathode inks were deposited by screen printing on each side of the YSZ discs and sintered in air for 120 min at 350 $^{o}$C and for 120 min (± 1 min) at 1200 $^{o}$C to

form the fuel cell. After sintering, the porous anode was impregnated with the cerium nitrate solution. The infiltrated ceria nitrates in the anode structures were calcinated in air at 800 $^{o}$C for 120 min (± 1 min) to decrease the surface area before further infiltration. After infiltration with the cobalt-copper solution and the cerium-cobalt solution, the cells were calcinated in air at 400 $^{o}$C for 120 min (± 1 min) to transform nitrates into oxides.

The primary concern with porous materials is the tendency of the metals to deposit non-uniformly, which potentially results in size growth and aggregation of particles. To solve this problem, the impregnated amounts of reducible catalysts (Cu and Co) were limited to below 15 wt% in total.

### 2.2 Fabrication and Treatment of the $BaCeO_3$-Based Materials

The experiment design is shown in Fig. 2.1. Fine and loose powders of a $BaCe_{0.7}Zr_{0.1}Y_{0.2}O_{3-\delta}$(BCZY) precursor were obtained by using a unique citrate-nitrate combustion method. First, citric acid was diluted in de-ionized water and used as a chelating agent for metal ions, and then 6.5335 g $Ba(NO_3)_2$, 7.5989 g $Ce(NO_3)_3 \cdot 6H_2O$, and 0.7831 g $ZrO(NO_3)_2 \cdot 4H_2O$ 1.9151 g (± 0.0005 g) $Y(NO_3)_3$ were dissolved in the solution with 14.4090 g citric acid. It was observed from the experiment that $ZrO(NO_3)_2 \cdot 4H_2O$ was hard to dissolve in the solution. The whole dissolution usually took more than half an hour. Then, 12.0000 g $NH_4NO_3$ was dissolved in the solution. The solution was heated until self-combustion occurred spontaneously as water evaporated. Powders thus obtained were then collected and heated in the furnace at 400 $^{o}$C for de-carbonization for 120 min (± 1 min).

The powder was ground and pressed into discs with thickness around 0.5 centimeter and sintered at 1200 $^{o}$C for 10 hours (± 1 min). Powders were then ball milled for 30 min (± 1 min) and final pellets were prepared by pressing at 200 Mpa and firing in air at 1550 $^{o}$C for 10 hours (± 1 min). The high temperature sintering resulted in a color change from pale yellow to brown. Some brown discs were ground again into fine powders for further processing and characterization.

Powders of $BaCe_{0.8}Y_{0.2}O_{3-\delta}$(BCY) and $BaZr_{0.8}Y_{0.2}O_{3-\delta}$(BZY) were fabricated in the same process and the degradation tests were conducted to study the degradation mechanism.

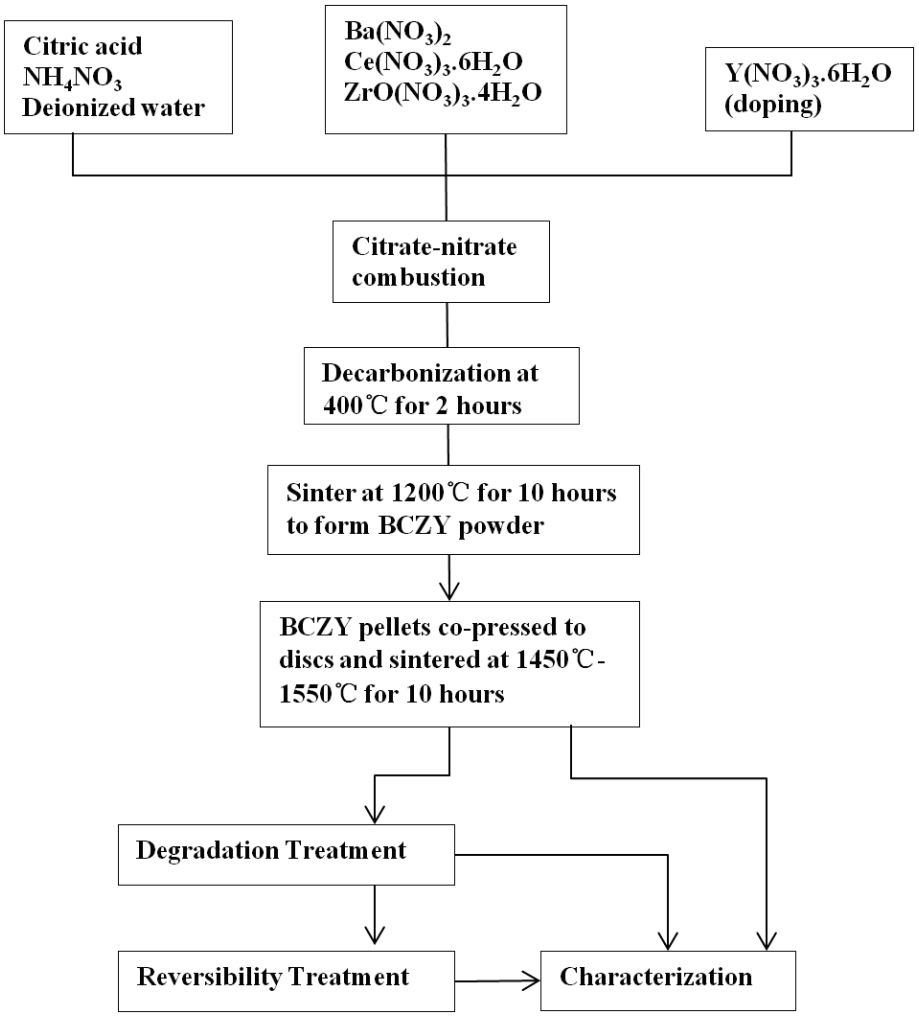


Fig. 2.1. Fabrication, degradation and reversibility treatment of BCZY.

Powders and discs of BCZY were treated in different degradation conditions.

The degradation treatments were performed in a quartz tube (Fig. 2.2) for 24 hours at room temperature (25 $^{o}$C). The samples were treated with wet/dry gases, including air and $CO_2$.

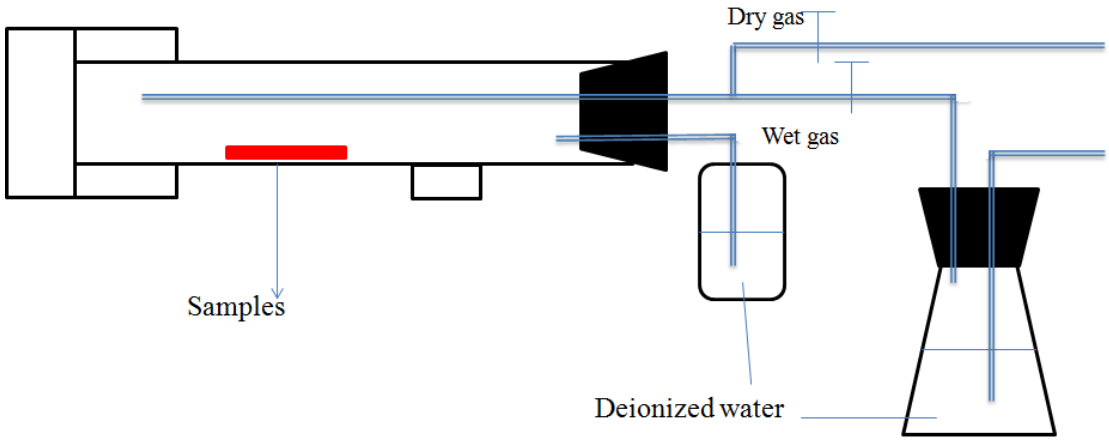


Fig. 2.2. Degradation treatment set-up.

The degraded specimens were ground and sintered at 1200 $^{o}$C for another 10 hours (± 1 min) to test the reversibility of the degradation.

**2.3 Set-up for Fuel Cell Measurements**

After the fuel cells were made, Au and Pt paste (mixtures of metals and terpineol) were attached to the surface of electrodes as current collector pastes for the anode and cathode, respectively. Au and Pt wires were applied to connect the current collector pastes to electrochemical workstation (Fig. 2.3). With the increase of temperature, the terpineol in the pastes was burned and the wires were connected to the metals left on the electrodes.

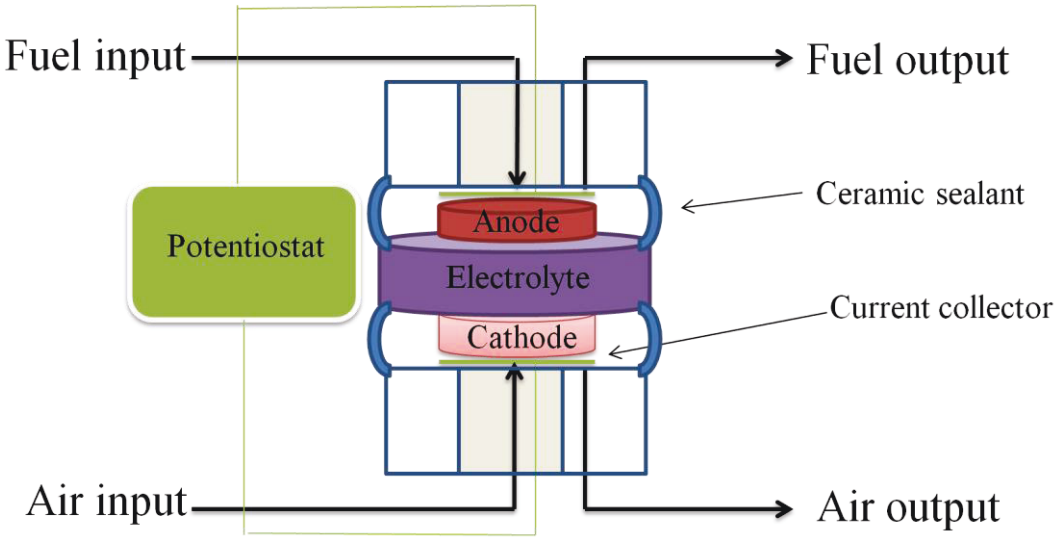


Fig. 2.3. Schematic of the set-up for fuel cell measurement.

Shown in Fig. 2.3, the SOFC setup with coaxial alumina tubes, inlet and outlet, was used for feeding fuel and air to the anode and the cathode of the cell. The outer tube of anode was sealed by the ceramic sealant (Ceramabond 503, Aremco) to adhere the fuel cell to the alumina tube and isolate an anode compartment from the cathode with the gas-tight electrolyte. In all single cell tests, gas was fed into the anode chamber at a flow rate of 25 milliliter per minute (ml $min^{-1}$), measured at 20 $^{o}$C under 2 Mpa, while air was supplied to the cathode chamber by exposing the cathode side to air. Once the ceramic sealant was cured, the fuel cell was heated to the operating temperature at a heating rate of 2 K per minute.

The fuels supplied to the anode were $H_2$ and syngas, which were stored in cylinders of compressed gases. A mass flow meter controller was used to adjust the flow rate.

### 2.4 Electrochemical Measurements

Electrode performance was investigated using an electrochemical workstation of a Solartron 1287 potentiostat and a Solartron 1255 frequency response analyzer.

### 2.4.1 Electrochemical Impedance Spectra

Electrochemical impedance spectroscopy (EIS) measures dielectric properties as a function of frequency. Impedance spectroscopy imposes a potential perturbation on a fuel cell and measures the current output. It allows one to distinguish between different losses/polarization processes and analyze the performance of a fuel cell with details. In general, there are three types of losses that contribute to the overpotential of a fuel cell at a given current density. These are ohmic losses, activation polarization losses and mass transfer losses.

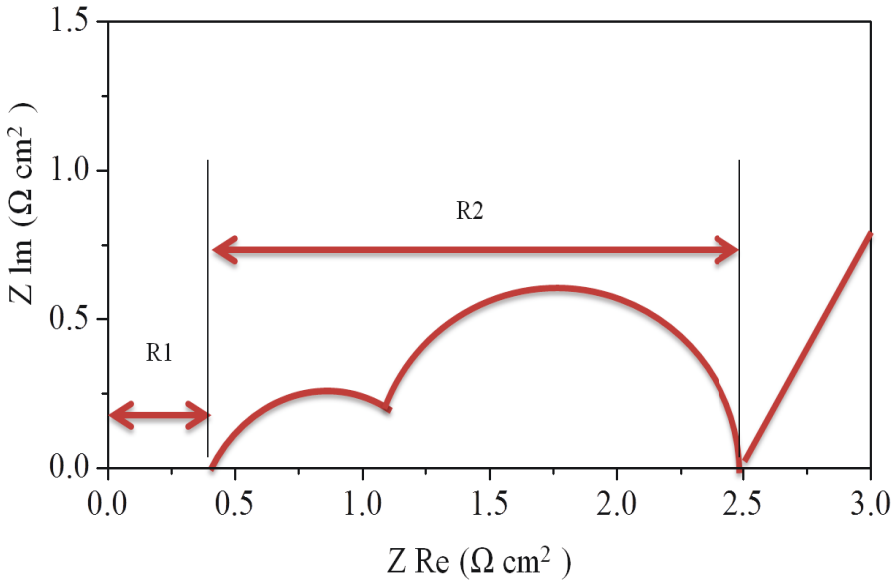


Fig. 2.4. Schematic of a typical EIS of SOFCs.

Fig. 2.4 is a typical example of an impedance spectrum obtained in a fuel cell. The x-axis intercepting with the curve at a high frequency represents the ohmic resistance R1, contributed by the resistances of electrolyte, electrodes and interconnects, among which the electrolyte usually contributes the most. Two arcs of R2 in the spectrum can be assigned to activation polarization of the cathode and the

anode. The mass transfer loss is represented by a small tail at frequencies under 1Hz.

In the experiments, the impedance spectra were recorded in the frequency range from $10^6$ Hz to 1 Hz, with AC perturbance of $\pm$20 mV.

### 2.4.2 Current Density-Voltage Curves

The j-V curve was measured with a potentiodynamic mode. The voltage was ramped from OCV voltage to zero at a rate of 5 millivolt per second ($mVs^{-1}$) or 10 $mVs^{-1}$. A four point probe measurement was used to ensure that the resistance of the interconnect was not included in the voltage losses of the cell. After measuring the j-V curve, j and power density (P) curve was calculated. Power density was acquired from multiplying voltage and current density, as shown in the equation: P = Vj (2.1). Potentiostatic mode was used to monitor the current stability at the set voltage of 0.7 V as a function of time.

## 2.5 Characterization Methods

### 2.5.1 Powder X-Ray Diffraction

Powder X-Ray diffraction (XRD) was used to determine the crystalline phase of materials. In addition to general components, lattice parameters, defects, and grain size of nano particles can be identified in a XRD test [34]. A beam of X-ray was diffracted by the crystalline atoms and the data on the interface of X-rays were collected at room temperature using monochromated Cu K$\alpha$ radiation source. Samples were scanned from 20 to 90$^o$ ($\theta$), and shown in a spectrum rate of 2$\theta$. Measurements were conducted soon after synthesis to minimize the influence of degradation.

### 2.5.2 Scanning Electron Microscopy

Scanning electron microscopy (SEM) is a powerful technique of achieving imaging information on surface morphology. To use this equipment, a high-energy beam of electron is scanned on a sample surface, generating signals such as secondary

electrons (SE) and backscattered electrons (BE). The SE signal is used mainly to obtain the images on the surface morphology whereas the BE signal is capable of providing compositional information [34]. Gold or carbon was sputtered onto the samples before the tests because the ceramics were un-conductive. Microstructure and morphology of particles, cross section and surface of cells were obtained at room temperature by a Hitachi S-2700 SEM.

### 2.5.3 X-ray Photoelectron Spectroscopy

X-ray photoelectron spectroscopy (XPS) determines the compositional, chemical and electronic state of a sample with the maximum thickness of 10 nm. A beam of X-rays is applied to irradiate a material and generate electrons. By measuring and analyzing the electrons, information on the electronic state is provided [34].

In this thesis, XPS was performed with a Kratos Analytical AXIS 165. A monochromated Al Ka (hv = 1486.6 eV) source was used under the pressure of 3 x $10^{-8}$ Pa. The obtained spectra were adjusted with the reference of C 1s before analysis.

### 2.5.4 Transmission Electron Microscopy and Energy Dispersive X-ray Spectrometer

Transmission electron microscopy (TEM) is a microscopy technique that transmits a beam of electrons through a thin specimen; the electrons interact with the specimen as they pass through and form images [34]. TEM analysis was performed with a JEOL 2010 microscope, operating at 200 kV accelerating voltage. The TEM observations were performed using a cryogenic holder held near 77 K. TEM samples were prepared by dispersing the powders in ethanol and dropping the liquid on amorphous carbon grids and in an argon glove box, directly before the TEM session.

Energy dispersive X-ray spectrometer (EDS) is an accessory usually coupled with TEM or SEM apparatus to analyze the elemental composition. The incident high energy beam of electrons excites an electron from an atom in the inner shell of the sample and the electron goes through the shell, creating an electron hole. The energy

difference between the inner and outer shell can be detected in the form of an X-ray, which determines the quantities of the elements by the intensity of X-ray radiation. Therefore, the element composition at the surface, as well as the quantities can be measured by EDS [34]. In this thesis, surface compositions of samples were determined using an EDS attached to TEM.

### 2.5.5 Thermogravimetric Analysis– Mass Spectometry

Thermogravimetric analysis (TGA) is a technique that analyzes the changes in physical and chemical properties as a function of increasing temperature. TGA is commonly applied to analyze loss/gain in weight and heat to reveal the chemical phenomena including decomposition, chemisorptions and dehydration, etc [34]. For this thesis, TGA was performed with a TA Instruments SDT Q600. The heating rate was 20 $^{o}$C per minute from room temperature to 1300 $^{o}$C.

The Mass spectometry (MS), thermostat QMS 200, was connected with the outlet of the flow of TGA as the input to analyze the formation of gaseous products as a function of temperature. MS is a technique for determining the chemical composition by the mass and charge characteristics in an electromagnetic field. The simple gaseous products can be ionized and analyzed through their mass to charge ratio efficiently.

### 2.5.6 Fourier Transform Infrared Spectroscope

Fourier transform infrared spectroscope (FT-IR) is a technique to obtain an infrared spectrum of absorption on a specimen. A beam of light with different frequencies/wavelength is applied to a sample and is partially absorbed. The absorption peak is determined by the vibrational energy gap, which stems from the vibrating molecules. The light absorption for each wavelength is then recorded through the fourier transform to identify the structure of molecules in gas, liquid and solid forms [34]. An ABB MB3000 Fourier Transformed Infrared was used to obtain the Spectra.

# Chapter 3 The Study of $La_{0.3}Sr_{0.2}Ba_{0.1}TiO_{3-\delta}$-based Anode Material Prepared by the Impregnation Method

## 3.1 Introduction

Ni/YSZ has been widely applied as the anode catalyst for $H_2$-fuelled SOFCs because of its excellent catalytic activity and electrical conductivity [35, 36, 37]. However, the inaccessibility of $H_2$ in nature limits the wide commercialization of $H_2$-fuelled SOFCs. Recently, the direct oxidation of light hydrocarbons in fuel cells has provided more economic benefits and attracted wide attentions from researchers.

Despite the excellent performances of Ni in pure hydrogen, it is not a proper anode catalyst operating in light hydrocarbons, since Ni catalyzes the formation of graphite and suffers metal-dusting caused structural disintegration of the anode [38].

One approach to enhancing carbon and sulfur resistance of anode catalysts is to replace Ni with perovskite materials. Lanthanum doped strontium titanate (LST) is a promising anode material since it exhibited excellent chemical stability even in sour hydrocarbons [39, 40, 41, 42]. With 40% of Sr sites occupied by La, which was the maximum level of substitution, a proportion of $Ti^{4+}$ is reduced to $Ti^{3+}$ to maintain the charge balance [43]. As a result, electronic and ionic conductivities were increased. Moreover, substitution of Sr with Ba could improve the ionic conductivity of the anode [44, 45]. However, the catalytic activity and electronic conductivities of the catalyst were insufficient to provide a high performance when compared with metallic anode catalysts.

To enhance the electrochemical performance of the anode without losing the integrity of the catalysts in hydrocarbons, the anode was separated into two distinct phases through infiltrating metallic catalysts into the perovskite-based substrate. It is widely known that the catalytic performance can be improved by providing highly dispersed nano-scale catalysts through the wet infiltration method that enhances the length of triple-phase boundaries (TPB) of an SOFC anode [40, 45, 46].

The choice of metallic catalysts was based on the study made by M. D. Gross [47]

who developed the Cu/Co catalyst to achieve a good balance between high catalytic activity and high chemical stability in methane. The addition of 5 vol% Co prepared by electrodeposition with Cu dramatically enhanced the performance without losing integrity in hydrocarbons, which was proved as an appropriate bi-metallic catalyst.

The schematic of the composite anode is shown in Fig. 3.1. The LSBT/YSZ provided a porous substrate which guaranteed an efficient diffusion of fuels and products. Nano-scaled metallic catalysts were uniformly distributed on the surface. Three types of infiltrates were investigated, as shown in Fig. 3.1. Infiltrates of Co and Cu were firstly investigated to enhance the performance of LSBT, with Co to enhance the catalytic activity and electronic conductivity and Cu to reduce carbon deposition. In the second approach, $CeO_2$ was pre-infiltrated to increase the redox and thermal stabilities of the infiltrates. Since it was revealed that $CeO_2$ also contributed to increasing carbon resistance, $Co/CeO_2$ was applied as infiltrates to achieve a balance of excellent performance and sufficient stability.

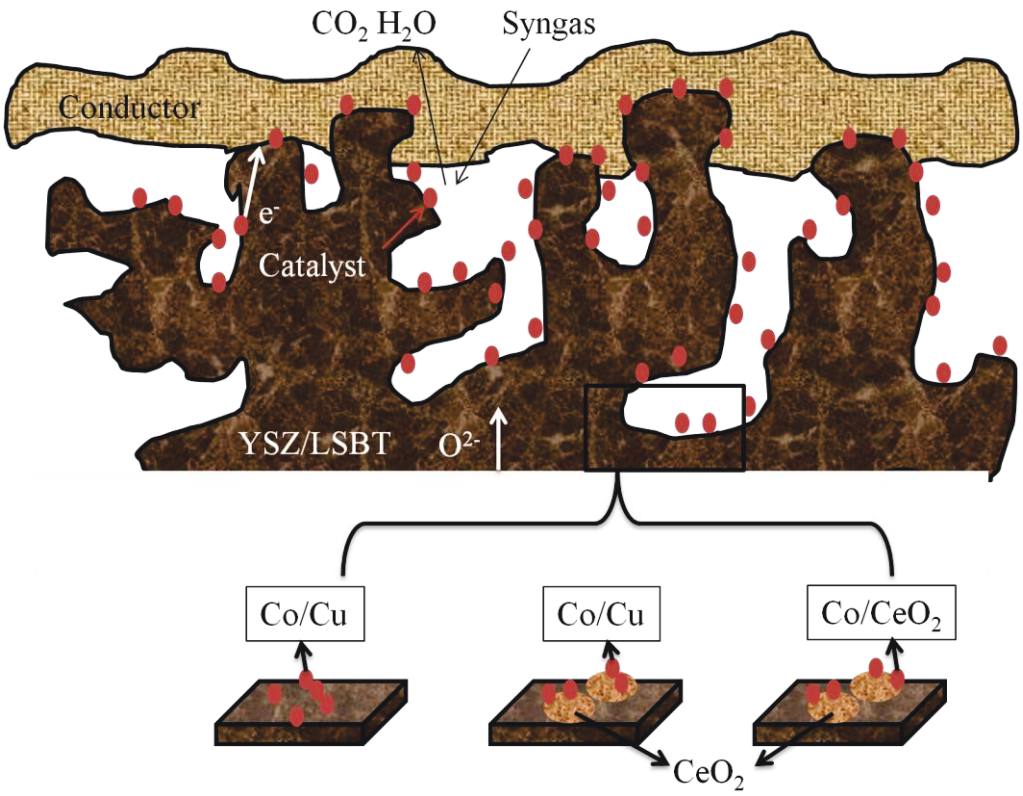


Fig. 3.1. Schematic of the composite anode and the design of experiments.

In this chapter, a LSBT-based anode substrate with dispersed catalyst was investigated to optimize the catalytic activities and the performance.

## 3.2 Results and Discussion

### 3.2.1 Morphology Analysis of SOFCs

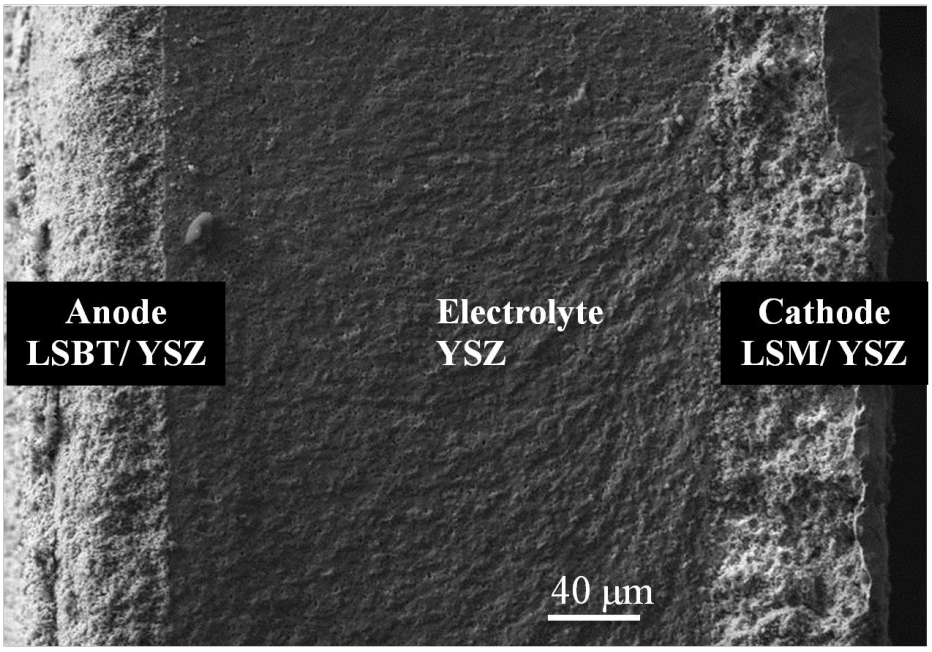


Fig. 3.2. SEM micrograph of the cross section of the SOFC with LSBT+YSZ/YSZ/LSM+YSZ.

Fig. 3.2 shows the cross section of a fuel cell with a porous anode on the left and a cathode on the right, both of which were firmly bonded to the dense electrolyte of 250 μm. The thicknesses of the anode and cathode were both around 60 μm. There were visible morphological changes at each surface of the electrodes, representing gold and platinum pastes as the current collectors for the anode and the cathode, respectively.

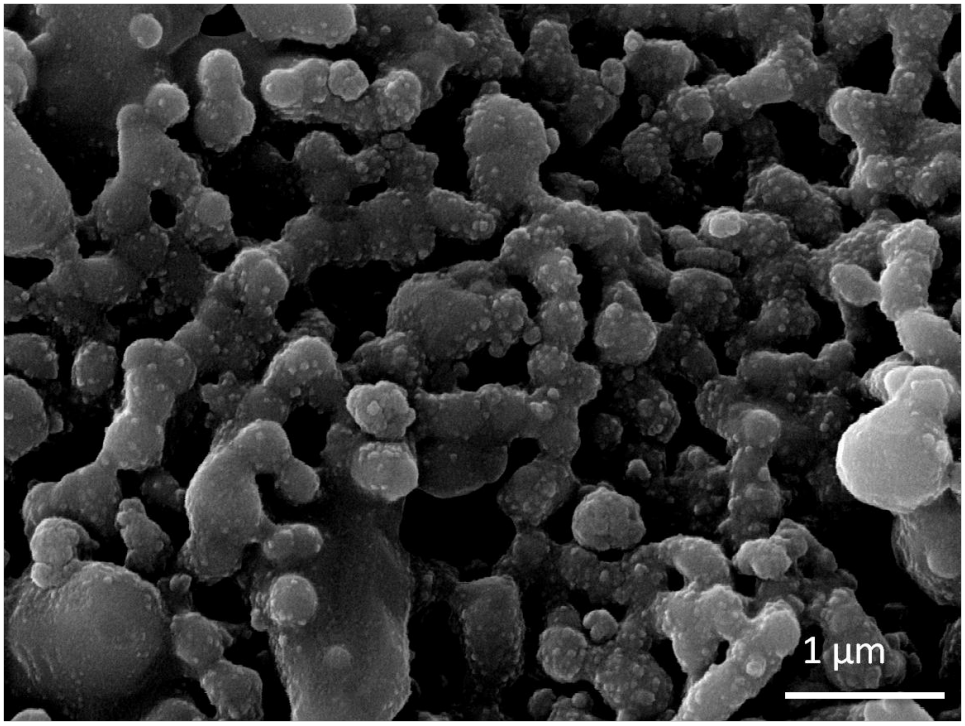


Fig. 3.3. SEM of the infiltrated LSBT+YSZ composite with 9.0 wt% $CeO_2$, 3.6 wt% Cu, and 5.4 wt% Co.

Fig. 3.3 exhibits the cross section of the anode with 9.0 wt% $CeO_2$, 3.6 wt% Cu, and 5.4 wt% Co. As shown in Fig. 3.3, the infiltrated particles appeared to be nano-scale. The fine microstructure and open porosity appeared to be favorable for a high performance anode. The microstructures of the anode remained consistent from sample to sample.

### 3.2.2 Electrochemical Characterization

#### 3.2.2.1 Electrochemical Analysis of Cu/Co Infiltration in LSBT

SOFCs with the LSBT/YSZ anode catalyst were infiltrated by 3.6 wt% Cu and 5.4 wt% Co and tested in $H_2$ at 950, 900 and 850 $^oC$. After the series of tests, the temperature was maintained at 850 $^oC$ for 30 min and then was set back to 950 $^oC$ and the cell was tested again. The objective of the comparison was to determine the thermal stability of the anode catalyst in $H_2$ as a function of time.

Electrochemical Impedance spectra provide more insight than I-V curves since they characterize different polarization processes. The electrochemical impedance spectra, shown in Fig. 3.4, were composed of two capacitance arcs which showed the activity polarization resistance of the catalysts. It was difficult to identify the individual activation polarizations of the cathode and the anode since there was no clear boundary between the two arcs. Nonetheless, an obvious increase in activation polarization occurred in the second test, reaching 1.2 Ω $cm^{-2}$ at 850 °C. The change in activation polarization loss as a function of time was a good measure of the loss of catalytic activity in the infiltrated anode. The degradation of the activation polarization performance, determined from the spectra, was evident and significant.

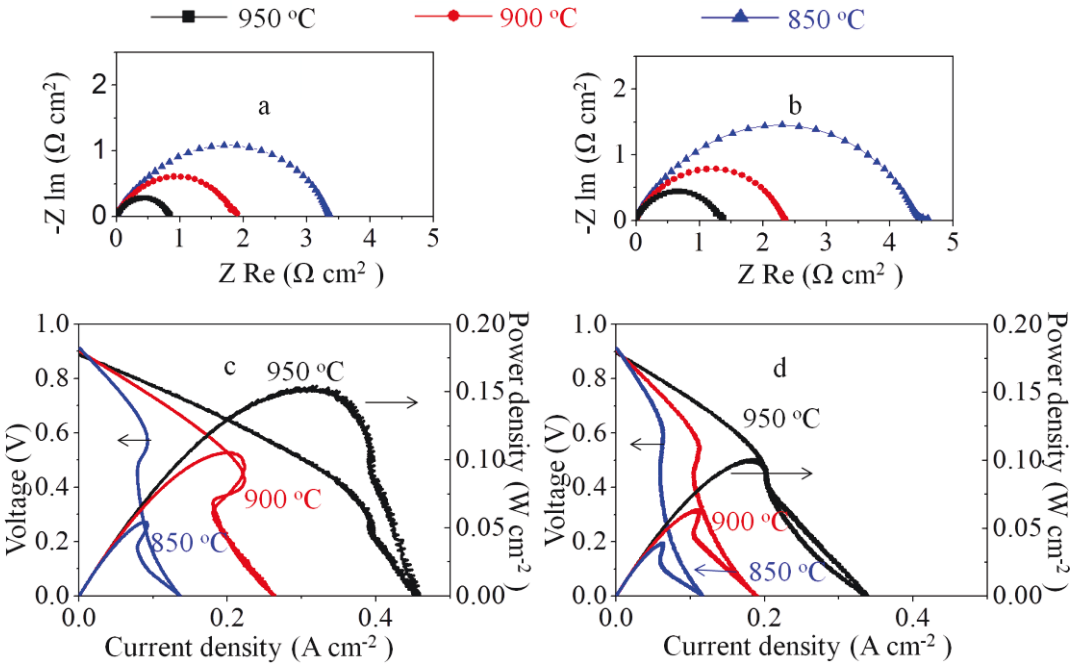


Fig. 3.4. EIS of of an SOFC with 3.6 wt% Cu, and 5.4 wt% Co infiltration in LSBT+YSZ anode in $H_2$, a. first time, b. second time; Electrochemical performance in $H_2$, c. first time, d. second time.

Potentiodynamic tests were conducted to determine the performance of the anode catalyst with Cu and Co co-infiltrated. Since the ohmic resistance of the cell was

mainly determined by the resistance of YSZ electrolyte, the ohmic resistance of the cell was calculated as 0.2 Ω $cm^{-2}$ at 850 $^{o}$C. However, the acquired ohmic resistance of the operating fuel cells was significantly higher than 0.2 Ω $cm^{-2}$. For the purpose of comparing the performance of the fuel cells, the ohmic resistances are all compensated in this chapter.

The power output was also reduced in the second test compared with the first one. Fuel cell performance was measured in $H_2$ and the results are shown in Figs. 3.4.c and d. It was observed that the j-V curve of the cell had two linear regions with different slopes that divided the j-V curve into a high voltage part and a low voltage part, with the slope change point at around 0.6 V. There was a sudden decrease in current density at the low voltage part. A possible explanation to the degradation observed is the oxidation of Co at low partial pressure of $H_2$ at TPB with the structural change of Cu and Co nano-particles [46]. Therefore, restraining the aggregation of dispersed particles was essential for a high performance anode catalyst.

3.2.2.2 Electrochemical Characterization of $CeO_2$/Cu/Co Infiltration in LSBT

To solve the problem of poor thermal stability, cells were pre-impregnated with cerium nitrate [49, 50] and sintered at 800 $^{o}$C before the infiltration of Co and Cu nitrates. The cells with infiltrated anode were tested in $H_2$ and syngas through electrochemical tests to find the optimal amount of metal loading in the anode. Figs. 3.5. a, c, e show the EIS results of the cells with the different amount of Co/Cu infiltrated in the anode in $H_2$, while Figs. 3.5. b, d, f exhibit the EIS results of the same cells operating in syngas. The activation polarization loss was significantly lower than that of the cell without $CeO_2$ infiltrated in LSBT substrates. The performance enhancement in the cell with $CeO_2$ infiltration can be attributed to the electrical and ionic conductivities that $CeO_2$ provided [49, 50]. With the increasing amount of infiltrated Co/Cu, the activation loss of the anode decreased within the range of low infiltration amount, and increased when the infiltrates exceeded certain amount [51]. The best performance of the cell was gained in the fuel cell with 9.0 wt%

ceria, 3.6 wt% Cu and 5.4 wt% Co infiltrates. The observed phenomenon can be attributed to the enhanced triple-phase boundaries caused by the increased amount of infiltrates. It is tentatively suggested that the infiltrated catalysts also reduced porosity of the electrode and blocked the gas diffusion pathway, resulting in negative effects on mass transfer [50]. When there was an excess amount of metal infiltrates, the length of the boundary was reduced and the performance of the anode was restrained [51].

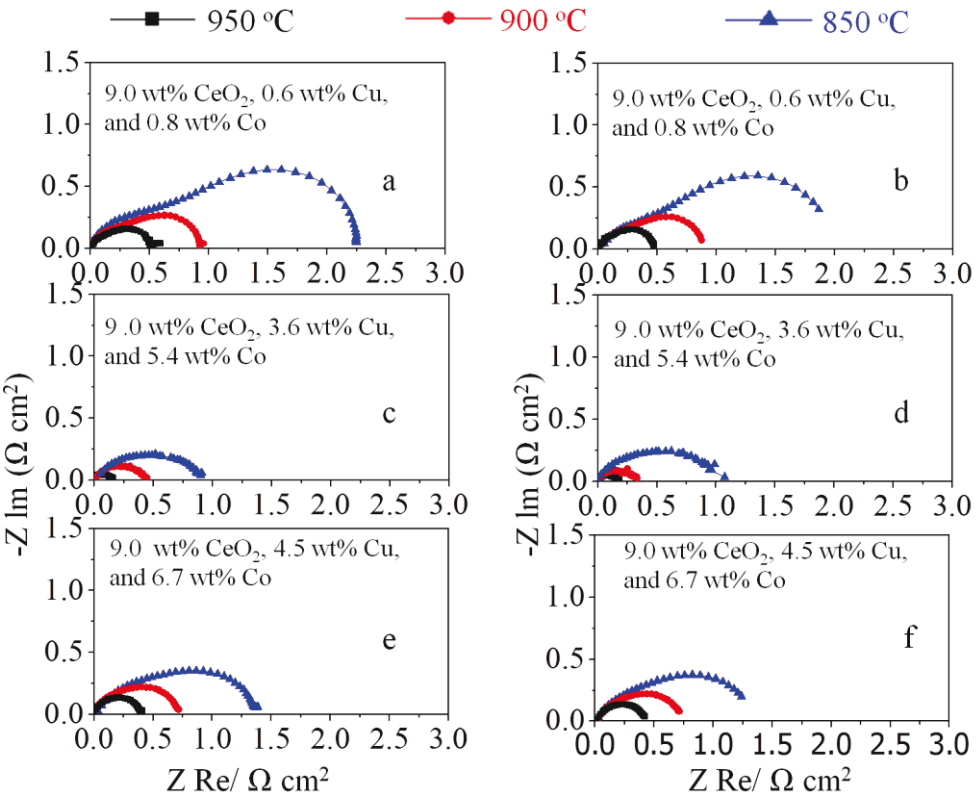


Fig. 3.5. EIS of SOFCs with $CeO_2$/Cu/Co infiltrated anode/YSZ/LSM+YSZ fed with different fuels: with 9.0 wt% $CeO_2$, 0.6 wt% Cu, and 0.8 wt% Co in a. $H_2$, b. syngas. 9.0 wt% $CeO_2$, 3.6 wt% Cu, and 5.4 wt% Co in c. $H_2$, d. syngas. 9.0 wt% $CeO_2$, 4.5 wt% Cu, and 6.7 wt% Co in e. $H_2$, f. syngas.

Fig. 3.6 exhibits the current density vs. voltalge and power density of SOFCs with a $CeO_2$/Cu/Co infiltrated anode. Generally the performance of the syngas-fed

SOFC is lower compared with the hydrogen-fed SOFC, and it was ascribed to catalytic activity [50, 51, 52] or the mass transport effect of CO. Since the combustion reactions were dominated by the multi-steps that involved the adsorption of fuel molecules on oxide at TPB and since hydrogen adsorbed more easily than CO, more negative effects on mass transfer influenced syngas-fuelled cells and eventually led to relatively poor performance [53].

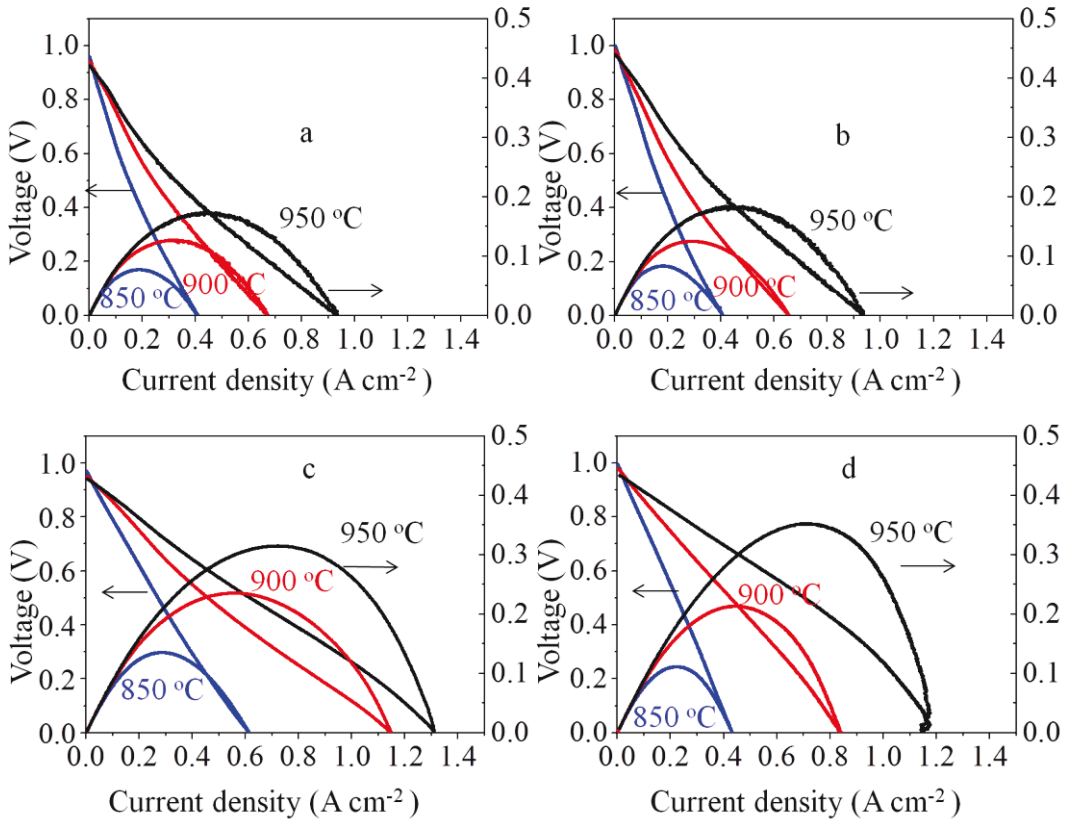


Fig. 3.6. Electrochemical performance of SOFCs with the anode infiltrated with 9.0 wt% $CeO_2$, 0.6 wt% Cu, and 0.8 wt% Co in a. $H_2$, b. syngas; with 9.0 wt% $CeO_2$, 4.5 wt% Cu, and 6.7 wt% Co in c. $H_2$, d. syngas.

Fig. 3.7 shows the j-V and power density-current density curves from 850 °C to 950 °C in dry $H_2$ and syngas for the fuel cells with the anode of 9.0 wt% $CeO_2$, 3.6 wt% Cu, and 5.4 wt% Co infiltration. The maximum power densities of the cell were 0.47 $Wcm^{-2}$ in hydrogen and 0.41 $Wcm^{-2}$ in syngas at 950 °C.

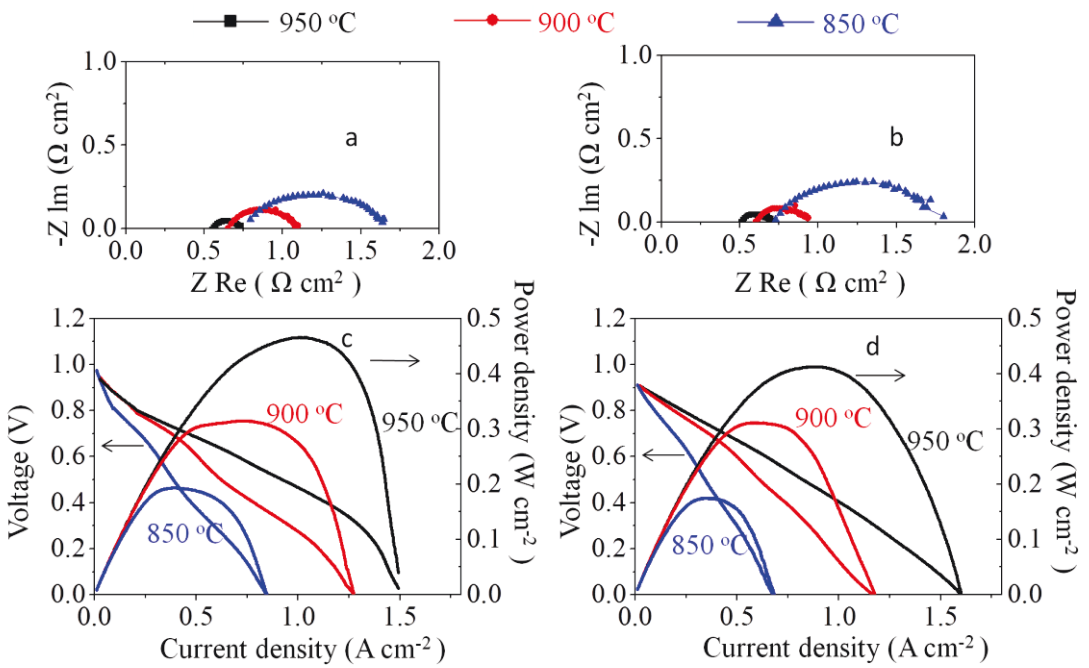


Fig. 3.7. EIS of an SOFC with 9.0 wt% $CeO_2$, 3.6 wt% Cu, and 5.4 wt% Co infiltration in LSBT+YSZ anode: a. in $H_2$, b. in syngas. Electrochemical performance c. in $H_2$, d. in syngas.

The OCV in dry $H_2$ varied from 0.935 to 0.974 V, while the OCV in syngas varied from 0.913 to 0.913 V, as shown in Figs 3.7. c and d, respectively. The ohmic losses changed from 0.562 to 0.794 Ω $cm^2$ from 950 °C to 850 °C in $H_2$, and from 0.522 to 0.727 Ω $cm^2$ from 950 °C to 850 °C in syngas. With performance presented, it was exhibited that the performance of the SOFC with the anode infiltrated with $CeO_2$, Cu and Co was greatly enhanced compared with the SOFC infiltrated with Cu and Co.

The electrochemical stability of the cell was investigated under potentiostatic condition in syngas at a fixed potential of 0.7 V, with the result shown in Fig. 3.8. There was an enhancement in performance in the first 10 min, followed by a steady degradation with the rate of 6.25 mA $cm^{-2}$ per hour. The enhancement of the performance possibly resulted from the carbon deposition influence, which enhanced

the electrical conductivity of the porous substrate [51, 54]. The degradation was explained by the morphology change due to either carbon deposition or sintering effect, as Cu possibly migrated to the surface of Co metallic catalyst [15].

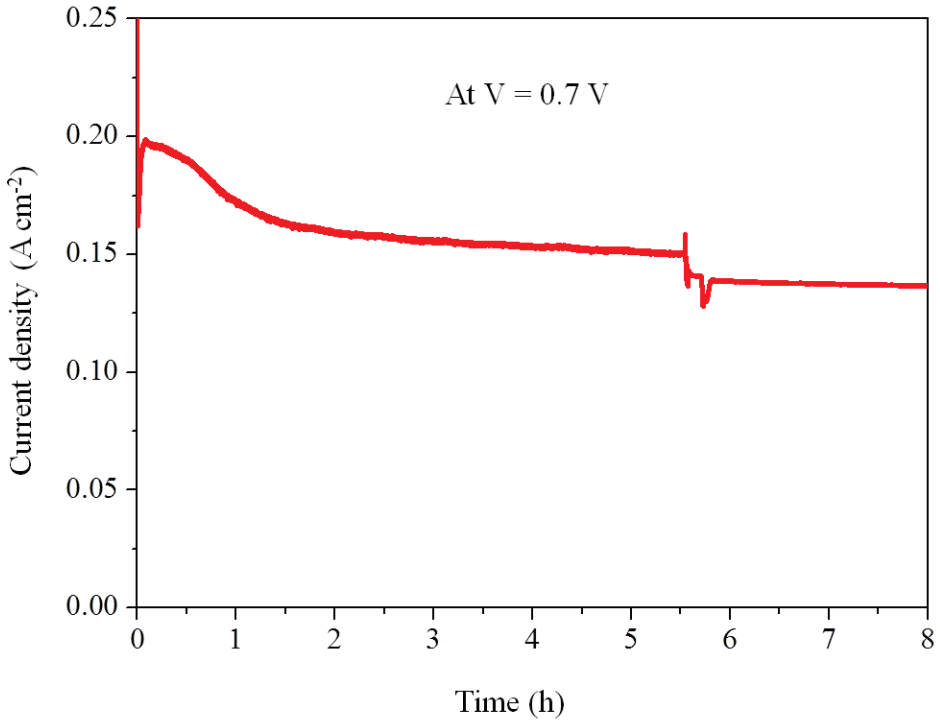


Fig. 3.8. Electrochemical stability test for the cell with LSBT+YSZ anode infiltrated with 9.0 wt% $CeO_2$, 3.6 wt% Cu, and 5.4 wt% Co at 850 $^oC$ in syngas.

### 3.2.2.3 Electrochemical Analysis of $CeO_2$/Co Infiltration in LSBT

$CeO_2$ was widely applied as to provide sufficient supporting substrates for infiltrated catalysts in SOFCs [53, 55]. To enhance the stability of the anode catalyst against carbon deposition and micro-structural change, Cu was replaced by $CeO_2$ and co-impregnated with Co into the LSBT/YSZ anode. Compared with Cu, $CeO_2$ enhanced the chemical and structural stabilities for the anode catalyst since it catalyzed the oxidation of carbon, and exhibited better redox and thermal stabilities. To investigate the effect of the amount of metal catalysts, different amounts of

$CeO_2$/Co were infiltrated into the anode substrate. Fig. 3.9 was obtained in $H_2$ and syngas from 950 °C to 850 °C. With the different amount of infiltrated $CeO_2$/Co, the best performance of the cell was reached at 10.5 wt% $CeO_2$ and 2.1 wt% Co infiltrates in the anode substrate.

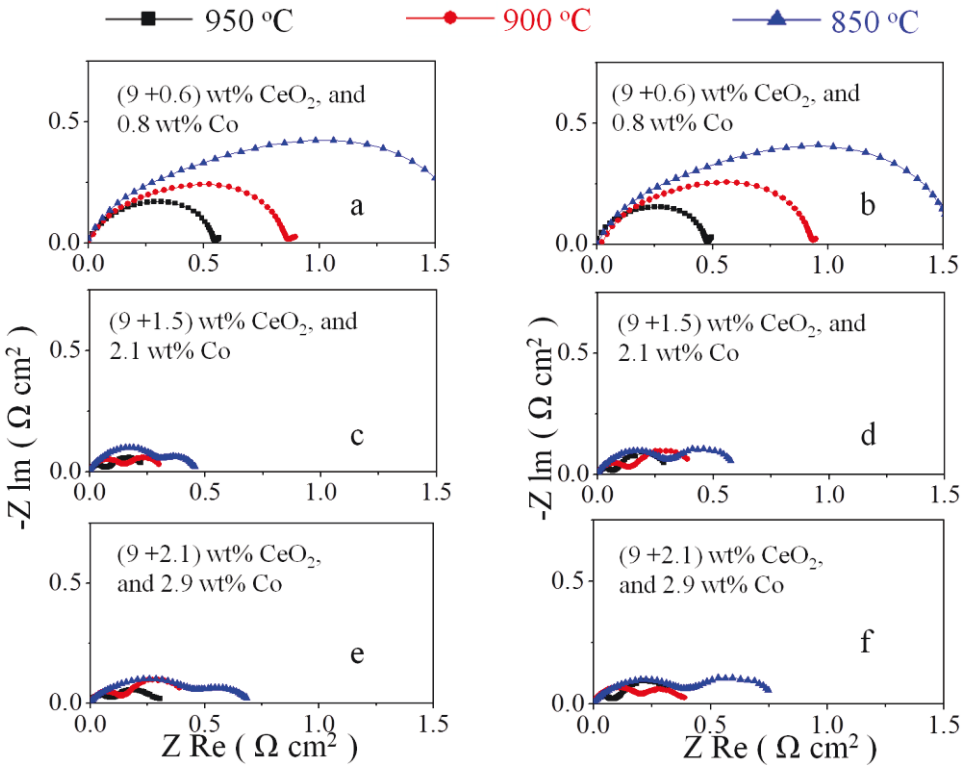


Fig. 3.9. EIS for $CeO_2$/Co infiltrated anode/YSZ/LSM+YSZ fed with different fuels, with the anode of 9.6 wt% $CeO_2$ and 0.8 wt% Co in a. $H_2$, b. syngas; the anode of 10.5 wt% $CeO_2$ and 2.1 wt% Co in c. $H_2$, d. syngas; the anode of 11.1 wt% $CeO_2$ and 2.9 wt% Co in e. $H_2$, f. syngas.

Fig. 3.10 exhibits the maximum power density of SOFCs with $CeO_2$/Co infiltrated anode. With the increased temperature, the power density increased, indicating that the reduction of activation polarization loss of electrode catalysts favored a higher temperature. Generally the performance of the anode catalyst increased with increasing amount of infiltrates due to the extension of the TPB length. However, with an excess amount of infiltrates, the active sites were blocked, resulting in a loss of activation activity. The sequence was confirmed in the anode infiltrated

with $CeO_2$/Co/Cu, as shown in Fig. 3.6.

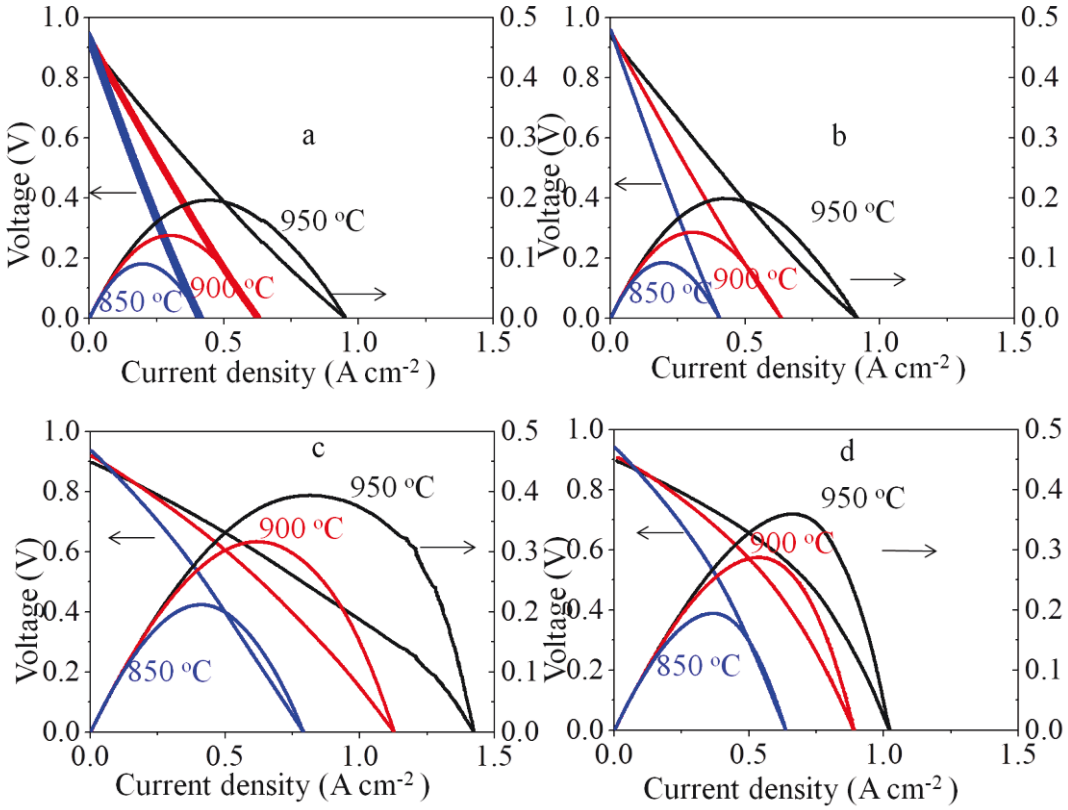


Fig. 3.10. Electrochemical performance of SOFCs with the anode infiltrated with. 9.6 wt% $CeO_2$, and 0.8 wt% Co in a. $H_2$, b. syngas; with 11.1 wt% $CeO_2$ and 2.9 wt% Co in c. $H_2$, d. syngas

The performances of the cell with 10.5 wt% ceria and 2.1 wt% Co in $H_2$ and in syngas are shown in Fig. 3.11. The overall performance of the cell with $CeO_2$/Co was enhanced, compared with the cell with $CeO_2$/Cu/Co, resulting from the enhancement of catalytic activity and increase of ionic conductivity provided by $CeO_2$.

The carbon resistance and thermal stability were investigated by electrochemical stability test in syngas at 850 °C at a fixed potential of 0.7 V, as shown in Fig. 3.12. Only a negligible decrease occurred within 24 hours. This indicated that the LSBT-based anode with 10.5 wt% $CeO_2$ and 2.1 wt% Co was electrochemically stable during 24 hours and the anode was not prone to the same degradation overtime that was discovered in $CeO_2$/Cu/Co infiltrated anodes. It is likely that the minor

performance degradation was attributed to the anode morphology change. .

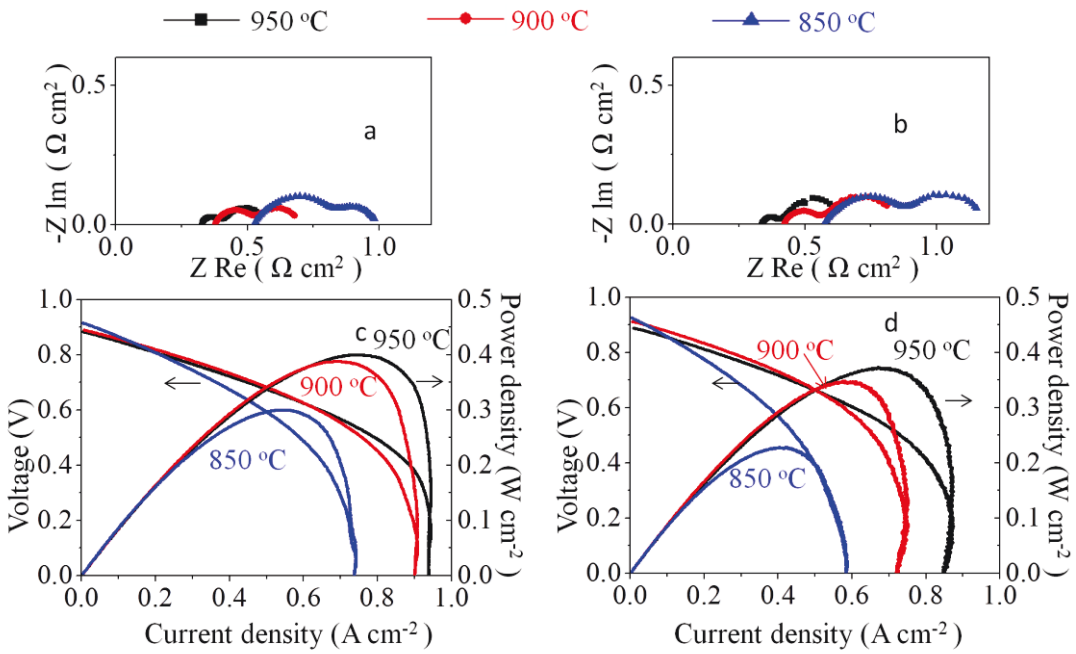


Fig. 3.11. EIS for the SOFC with 10.5 wt% ceria, and 2.1 wt% Co infiltrated in LSBT+YSZ anode in a. $H_2$, b. syngas. Electrochemical performances in c. $H_2$, d. syngas.

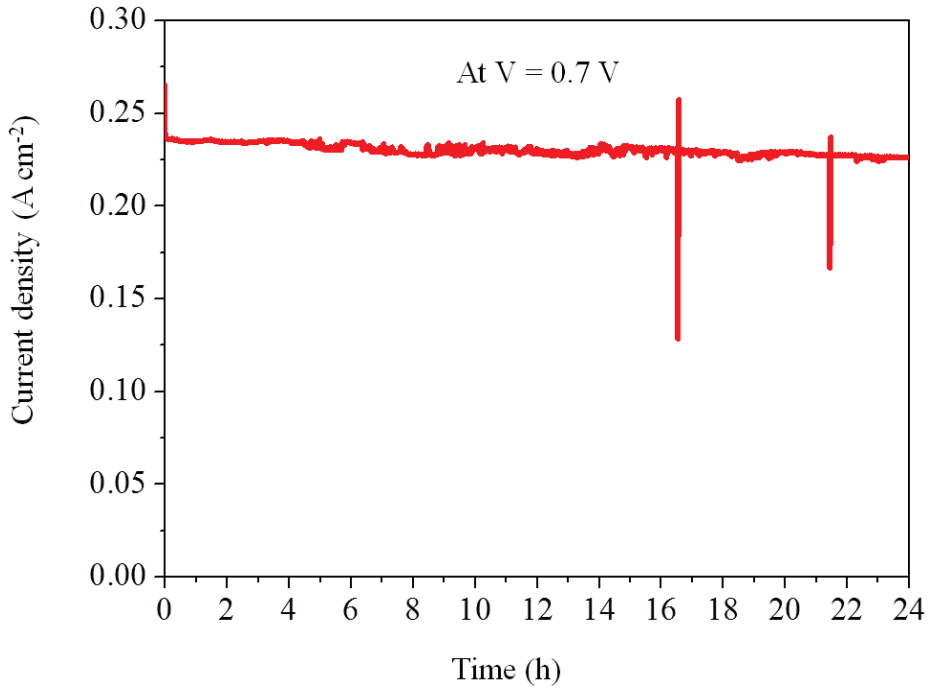


Fig. 3.12. Electrochemical stability test for the cell with LSBT+YSZ anode infiltrated with 10.5 wt% $CeO_2$ and 2.1 wt% Co at 850 $^oC$ in syngas.

# Chapter 4 Study of Degradation of Proton-conducting Material- $BaCe_{0.7}Zr_{0.1}Y_{0.2}O_{3-\delta}$ at Room Temperature

## 4.1 Introduction

In the temperature range of 550 $^{o}$C to 800 $^{o}$C, the $BaCe_{0.7}Zr_{0.1}Y_{0.2}O_{3-\delta}$ has been widely applied as the proton conducting material for SOFCs [56, 57, 58]. Formulated from Y-doped $BaCeO_3$ and $BaZrO_3$ solid solution, BCZY has been proposed as a good candidate for an electrolyte that sustains a good balance between high electrical conductivity and sufficient chemical stability [58]: it exhibits excellent proton conductivity due to the contribution of $BaCeO_3$ whereas $BaZrO_3$ provides good chemical stability in $CO_2$ and steam-containing gases [58, 59, 60, 61].

The stability of BCZY at room temperature received attention from our group in the process of formulating electrolyte supporting discs. The BCZY discs went through a sintering process in air at 1550 $^{o}$C to 1650 $^{o}$C for 10 hours to form a stabilized cubic perovskite structure with enhanced ionic conductivity [58, 60]. However, the mechanical and electrical properties spontaneously and severely degraded over time at room temperature. Although the degradation of BCZY in acidic gases and steam at high temperature has been intensively investigated [58, 59, 60, 61], there has been, to my best knowledge, no research on the degradation of BCZY at room temperature, so the mechanisms have not been understood.

In this chapter, BCZY degradation was investigated. A detailed study of the changes in the structure of BZCY before and after the degradation treatment and reversibility tests was carried out. A hypothesis on the degradation mechanism was proposed based on the experimental results.

## 4.2 Results and Discussion

### 4.2.1 Phenomenological Observations and SEM Analysis of the Degradation

The surface morphology of the fresh BCZY disc is shown in Fig. 4.1. a. The

degraded BCZY disc that went through the degradation treatment for 24 hours and the ground BCZY powders from the degraded BCZY disc are presented in Figs. 4.1.b and c. Compared with the compact surface of the fresh BCZY disc in Fig. 4.1.a, the boundaries of the disc in Fig. 4.1.b were weakened and cracks appeared at the surface that acted as a source of macro-cracks. These changes were defined as the "brittle fracture" owing to the observed pattern. Fig. 4.1.c exhibits rod-shaped pieces resulting from the "efflorescence" of the bulk BCZY powders. The pieces were nano-scaled with lengths ranging from 0.1μm to 0.9 μm.

The SEM results confirmed the phenomenon observed from Macroscopic-scale that BCZY discs cracked at room temperature. To study the mechanisms, further characterizations were conducted.

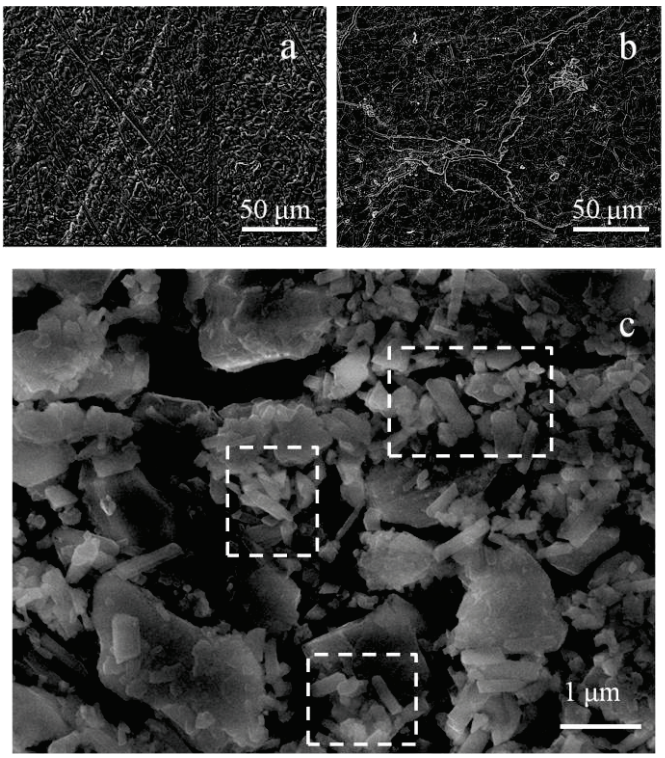


Fig. 4.1. SEM images of a. the fresh and b. the degraded BCZY discs, and, c the grilled BCZY powders, with white frames indicating the formation of the new phase.

### 4.2.2 XRD Analysis of the Degradation of BCZY, BCY, and BZY

XRD analyses were performed on the BCZY powders treated under different conditions. Fig. 4.2 shows the XRD patterns for a: the fresh BCZY and BCZY treated in b: 100% Air; c: 100% $CO_2$; d: 3%$H_2O$+97% Air and e: 3% $H_2O$+97% $CO_2$.

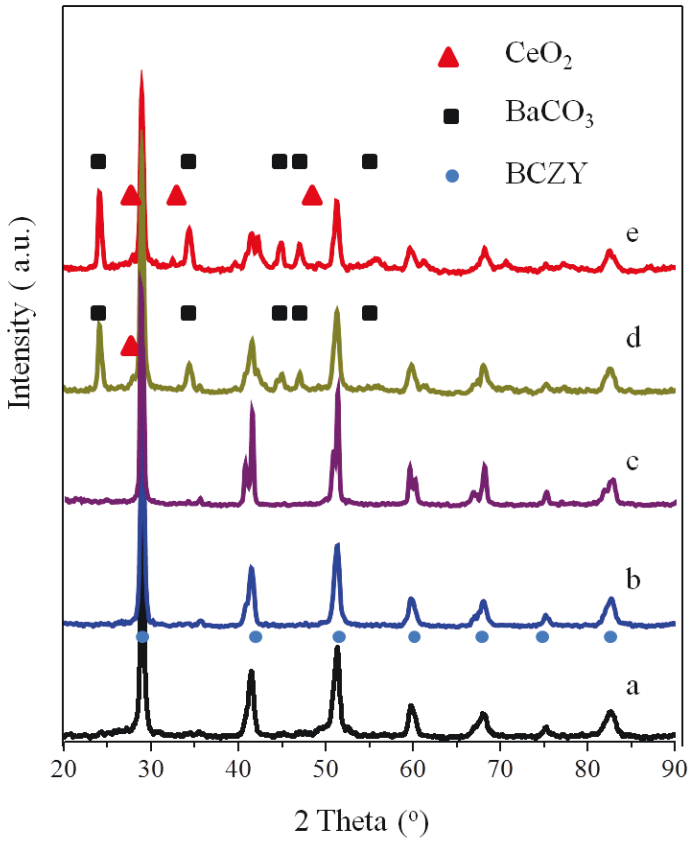


Fig. 4.2. The XRD patterns of a. fresh BCZY, and BCZY treated in b. 100% Air, c. 100% $CO_2$, d. 3%$H_2O$+97% Air, and e. 3% $H_2O$+97% $CO_2$.

The XRD pattern of the fresh BCZY displayed an orthorhombic phase which was identical from Figs. 4.2. a to e. Composition changes were discovered only in degradation treatment with the wet gases. Thus, a conclusion can be drawn that water vapour played a crucial role in the degradation process. The presence of $BaCO_3$ in

Figs. 4.2. e and f implied that $CO_2$ also contributed to the degradation process, yet $CO_2$ did not function by itself, as shown in the XRD pattern of the unchanged composition of BCZY in c. Compared with Fig. 4.2. d, the intensity of $BaCO_3$ in Fig. 4.2. e tended to be stronger, which implied that $CO_2$ and $H_2O$ were the major components contributing to the degradation of BCZY. In addition to $BaCO_3$, a minor amount of $CeO_2$ was also detected in Figs. 4.2. d and e.

In the solid solution of BCY and BZY, both were likely to suffer the degradation observed, therefore, degradation tests were conducted on BCY and BZY with the results shown in Figs. 4.3 and 4.4. The formation of $BaCO_3$ was inevitable during the degradation tests in both BCY and BZY. Compared with BZY, BCY was significantly more vulnerable to the degradation. The BZY was relatively stable during the degradation treatment, with a negligible amount of $BaCO_3$ formed in the process. The results suggest that BCY was comparably more prone to degradation, which was also observed at an elevated temperature in acidic gases [57, 58, 59, 60]. The cell refinement was conducted to calculate the precise lattice constants: in fresh BCY, the lattice parameters a, b, and c (the physical dimensions of unit cell in a crystal lattice) were 8.778 Angstrom (Å), 6.206 Å and 6.200 Å, while in degraded BCY, the lattice parameters a, b, and c were 8.748 Å, 6.279 Å and 6.237 Å. The result implied that although the formation of $BaCO_3$ was inevitable, the lattice dimensions of BCZY almost remained the same.

According to the calculation of HSC 5.0, $BaCeO_3$ was thermodynamically vulnerable to $CO_2$ and steam at room temperature. Thus, the degradation possibly started with steam and proceeded with $CO_2$.

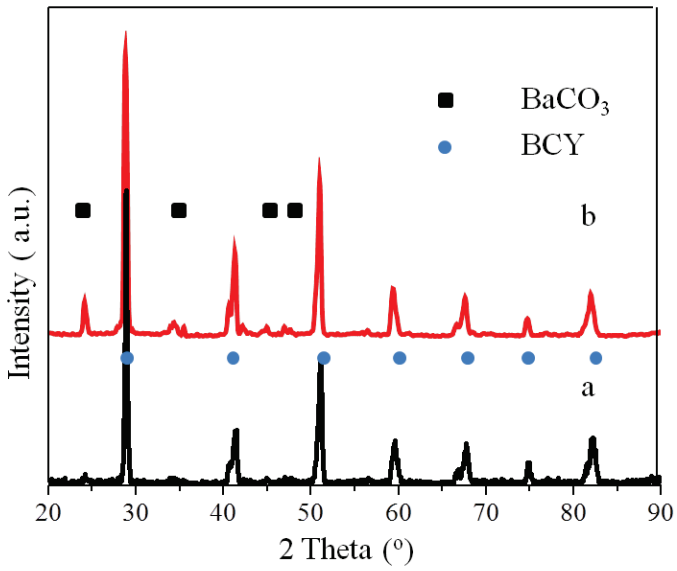


Fig. 4.3. The XRD patterns of a. fresh BCY, b. BCY treated by 3% $H_2O$+97% Air.

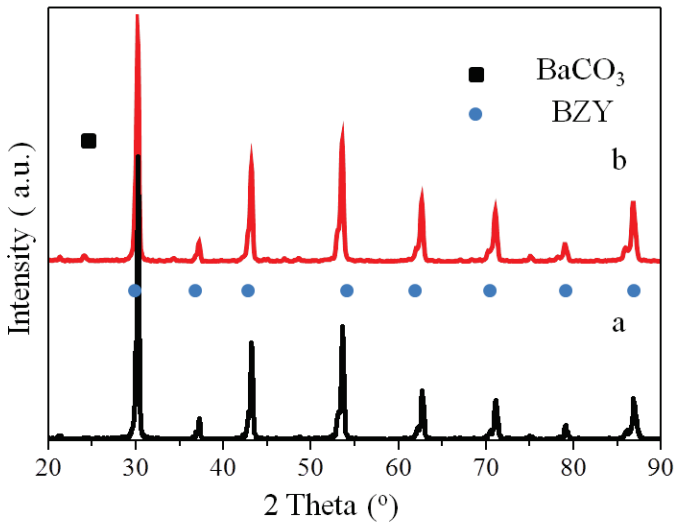


Fig. 4.4. The XRD patterns of a. fresh BZY, b. BZY treated by 3% $H_2O$+97% Air.

Figs. 4.5 proves the reversibility of the degradation. The XRD patterns show that the high temperature transformed the degraded sample into perovskite structure, with each peak fitting the XRD pattern of the fresh BCZY. The result reveals that the degradation of BCZY was reversible.

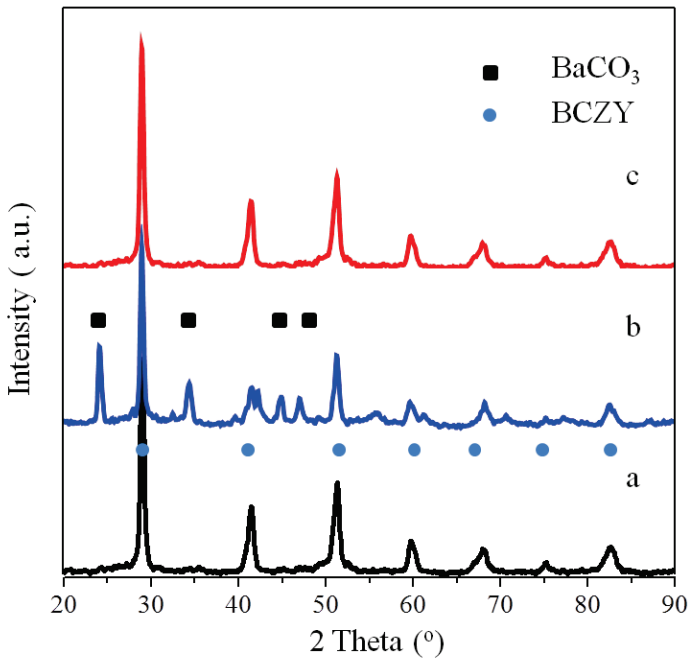


Fig. 4.5. The XRD patterns of a. fresh BCZY, b. BCZY treated in 3% $H_2O$+97% Air, c. BCZY treated in 3% $H_2O$+97% Air and then sintered at 1200 $^oC$ for 10 hours.

### 4.2.3 TEM Analysis of Fresh and Degraded BCZY

The fresh and degraded BCZY powders were ground and dispersed in ethanol, and the dispersed powders went through the TEM analyses. Rod-shaped

nano-particles, shown in Fig. 4.6. a, were discovered, which were identified as single crystals by selected area electron diffraction (SAED) analysis in Fig. 4.6. b. The SAED pattern reveals that the rod-shaped particles had an orthorhombic structure with the strong crystallographic orientation.

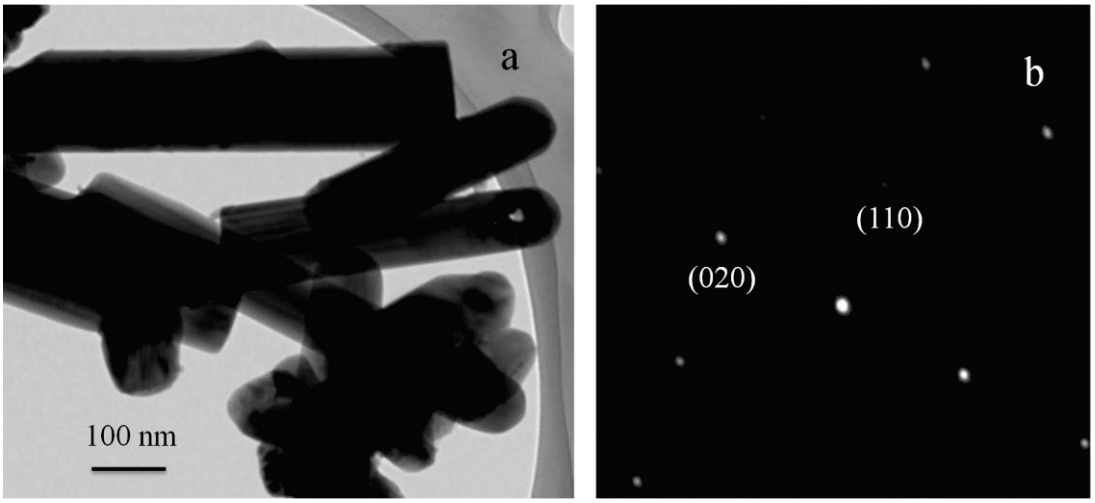


Fig. 4.6. a. TEM image of rod-shaped powders in degraded BCZY, b. SAED pattern.

The EDS analysis was carried out to determine the composition at elemental scale to study the composition of the original BCZY compared with the composition of the new phase, as shown in Figs. 4.7 and 4.8, respectively.

Since the main peaks for energy loss of Ce are close to the peaks of Ba, the distributions of elements were indicated only on Ba, Zr, Y and C. The existence of a Cu peak came from the porous Cu mesh, which was excluded from the elemental composition of the specimens.

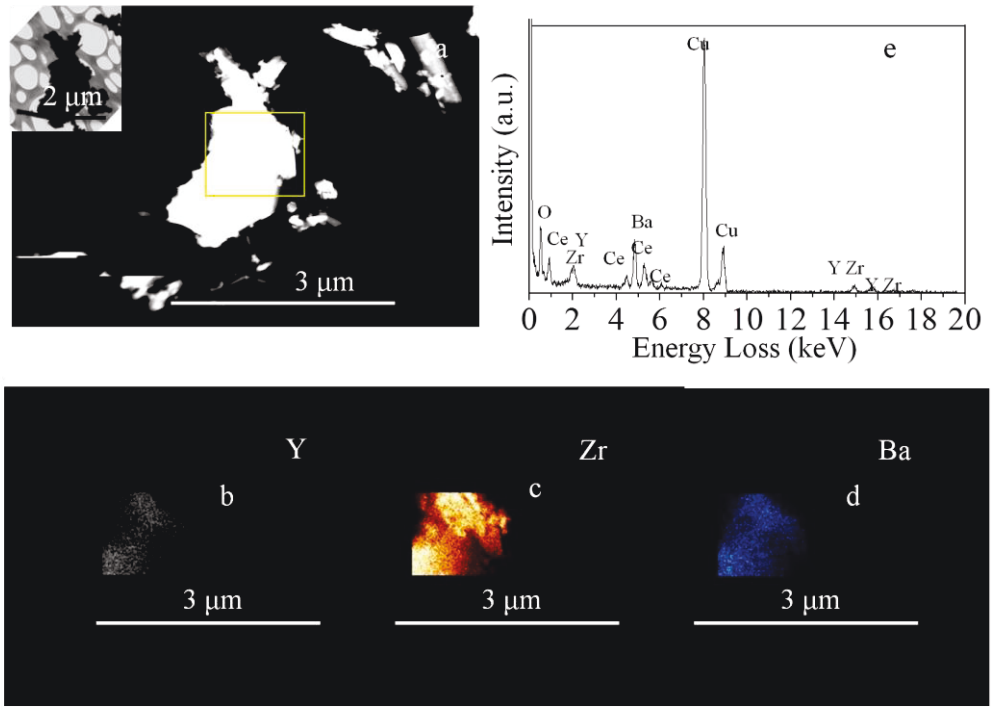


Fig. 4.7. a. Scanning TEM (STEM) image of bulk powder, with element maps of b. Y, c. Zr, d. Ba, and e. EDS spectrum.

Figs. 4.7. b, c and d reveal that Ba, Zr and Y were each distributed uniformly and homogenously on the surface of the original BCZY composed of Ba, Ce, Zr, Y and O.

The main elements discovered in the rod-shaped powders in the degraded BCZY were C, O and Ba (Figs. 4.8. b, c, d, e, f) with the single crystal structure confirmed in Fig. 4.6. b. The formation of $BaCO_3$ was evident, with labeled spots corresponding to the crystal planes of (020) and (110), which matches the structure of $BaCO_3$. The composition spectrum shown in Fig. 4.8. f implies that the formation of $BaCO_3$ was abundant and segregated.

There was no united $CeO_2$ detected from the degraded sample (Fig. 4.8. f). Since the peaks of $CeO_2$ shown in the XRD results of the degraded specimen were also negligible, this suggests that the formation of $CeO_2$, unlike $BaCO_3$, was dispersed.

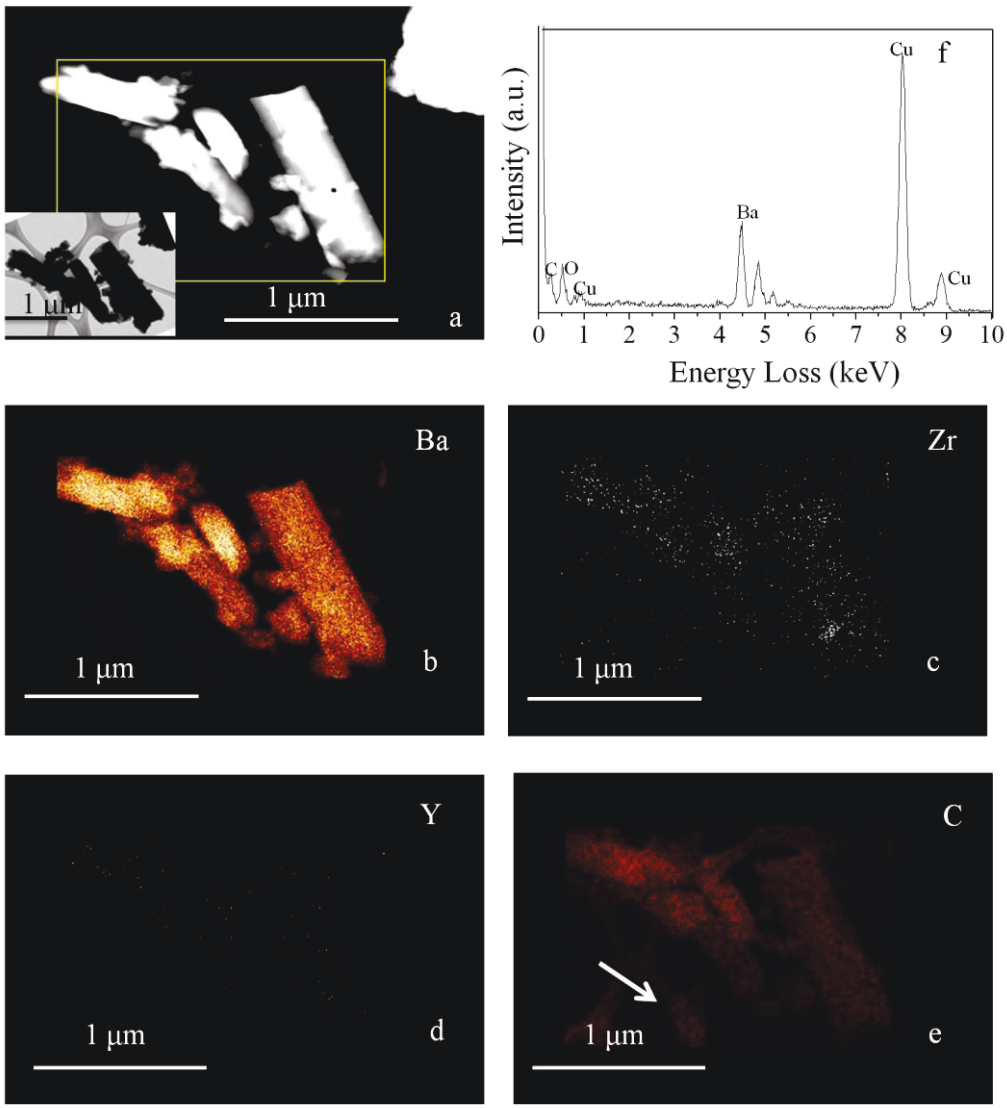


Fig. 4.8. a. STEM image of rod-shaped powder, with chemical maps of b. Ba, c. Zr, d. Y, e. C, and f. EDS spectrum, with the arrow indicating the carbon grid.

### 4.2.4 XPS Analysis of the Fresh and Degraded BCZY

The valance states of the isolated elements in the fresh disc of BCZY were compared to those in the degraded disc using XPS analysis. To avoid contaminating the fracture surface of discs by the water vapour in the air, the discs were placed with desiccants in a chamber for less than 24 hours before being transferred into the spectrometer where the XPS analyses were performed.

Fig. 4.9 shows the characteristic peaks of $3d_{5/2}$ with the binding energies of $Ba^{2+}$

at 779.9 eV and 795 eV in fresh and degraded BCZY [62]. Compared to the fresh BCZY as the reference specimen, the difference in the relative intensities of the peaks for the degraded specimen was negligible.

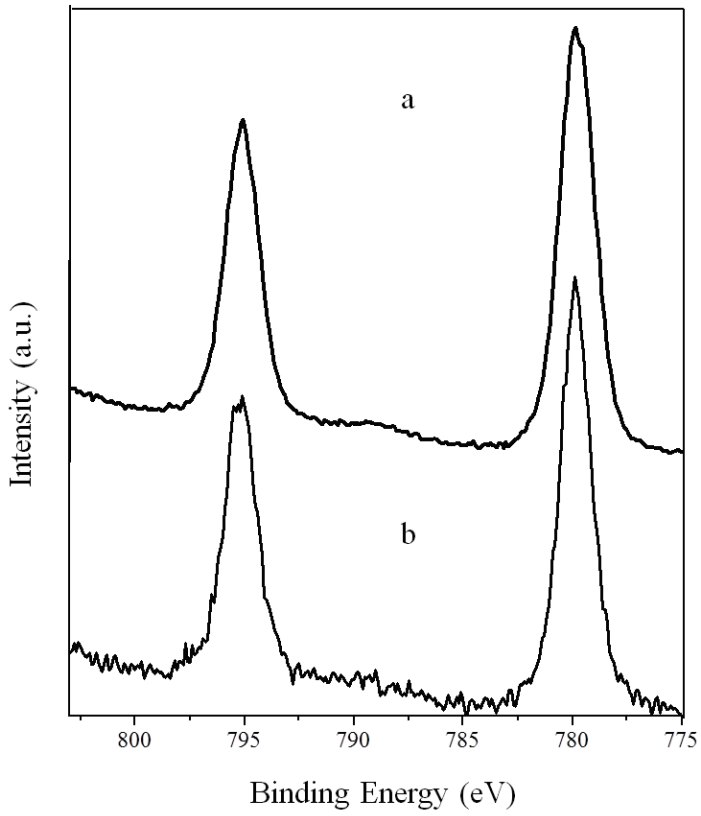


Fig. 4.9. Ba 3d XPS spectra of a. the reference specimen, and b. the degraded specimen.

The XPS result of Ce was more complicated owing to the multiple satellite peaks and the two typical chemical states of $Ce^{4+}$ and $Ce^{3+}$. Fig. 4.10 reveals that some curves of Ce 3d were caused by peaks of Ba, making the XPS results more complicated to be analyzed. The bonding energies of 916.7 eV, 898.3 eV and 882.3 eV [63, 64, 65, 66] corresponding to the characteristic peaks of Ce $3d_{5/2}$ at 4+ (formation of $CeO_2$) increased significantly due to the degradation treatment.

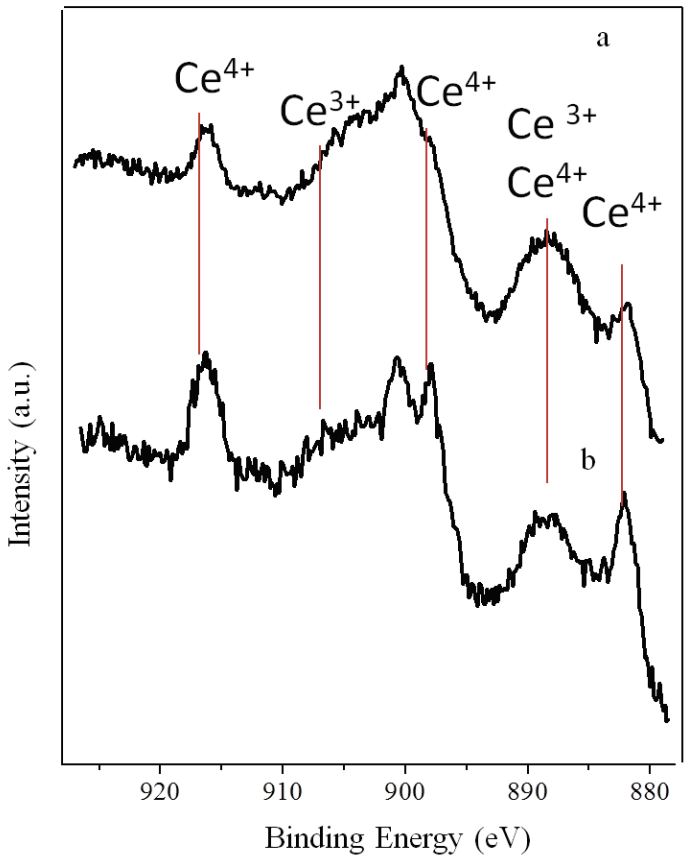


Fig. 4.10. Ce 3d XPS spectra of a. the reference specimen, and b. the degraded specimen.

The O1s XPS spectra measured for the reference specimen and the degraded specimen are given in Fig. 4.11. Two distinctive peaks were found in each spectrum. The peak at the lower binding energy (529.4 eV) was characterized as = O, while the characteristic peak at the higher binding energy (531.4 eV) resembled the typical – OH [65] and stemmed from the – OH adsorbed on the sample. The result implies that the ratio of O 1s in hydroxide decreased, resulting from the formation of oxides after exposure to wet air during the degradation treatment. In the fresh sample of BCZY, except for the $OH^-$ from the water vapour adsorption, part of the – OH may possibly come from the steam that diffused into the interior of the specimen through the micro-fractures on the surface. The results of the degraded sample imply that the – OH transformed into $O^{-2}$ during the degradation process.

Fig. 4.12 suggests that the intensity of Y 3d [66, 67] in the degraded sample was relatively weak, rendering the peaks invalid for investigation. The reduced intensity of the degraded sample was resulted from the formation of new components at the surface. It was assumed that the introduction of Y possibly enhanced the concentration of oxygen vacancies in the wet atmosphere [56, 68], which resulted in the adsorption of – OH onto the surface. The increased defects and reduced symmetry of the cubic perovskite structure could result in the degradation of the perovskite.

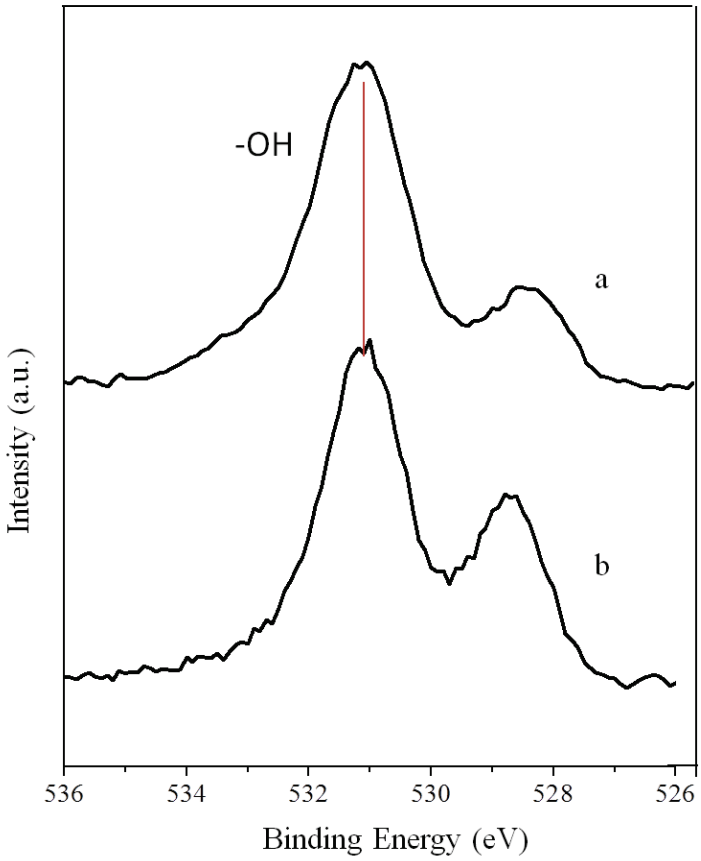


Fig. 4.11. O 1s XPS spectra of a. the reference specimen, and b. the degraded specimen.

The XPS results suggest that water vapour resulted in the formation of Ce–OH, Ba–OH and Y–OH bonds. Such features possibly rendered the grain boundaries vulnerable to the $OH^-$ attack and caused the initialization of degradation.

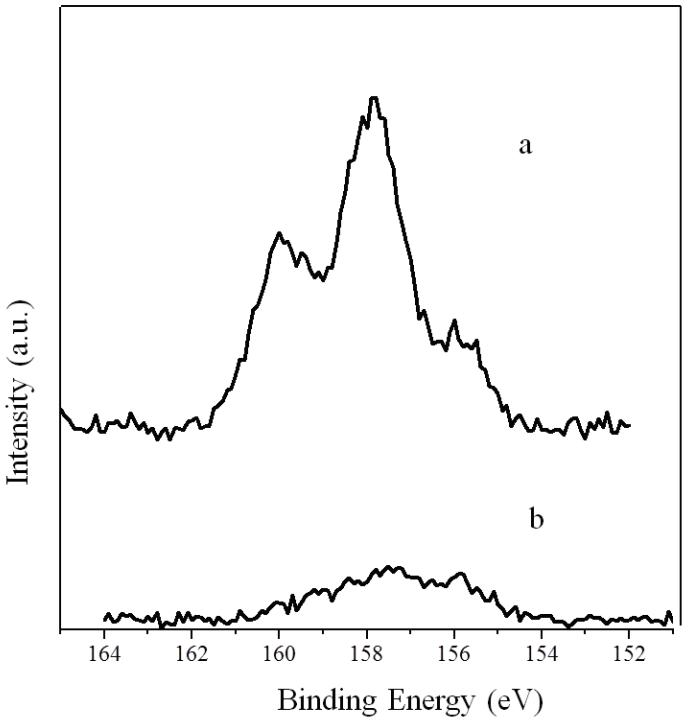


Fig. 4.12. Y 3d XPS spectra of a. the reference specimen, and b. the degraded specimen.

### 4.2.5 Analysis on Degradation and Reversibility Treatment

Figs. 4.13. a and b present the weight change and differential thermal analysis (DTA) curves of the fresh BCZY and the degraded BCZY treated through thermogravimetry analysis in air. The DTA curve of the degraded BCZY in Fig. 4.13 b exhibits the two main endothermic peaks with the first step occurring at about 800 $^{o}$C and the second one occurring at about 1000 $^{o}$C, while the DTA curve of the fresh sample exhibits no endothermic peak below 1000 $^{o}$C.

There was a total of 2% weight loss in the weight of the fresh specimen, which resulted from the loss of non-stoichiometric O in the perovskite structure with the increase of temperature [69, 70]. For the degraded sample, on the other hand, there were three main weight losses from the temperature programmed analysis. The first weight loss was mainly contributed by the evaporation of physically adsorbed water,

hydroxyle groups and adsorbed species since there was no DTA peak in the range, illustrating that no chemical reaction occurred in the process. The second steep weight loss was attributed to the decomposition of carbonates due to a DTA peak at the same temperature. The third steep weight loss mainly corresponded to the decomposition of $BaCO_3$: the sample revealed a weight loss platform at around 1000 $^oC$ that matched the decomposition temperature of $BaCO_3$.

The temperature program in thermogravimetric analysis also explains the reversibility of degraded BCZY. The results of the TGA illustrate the decomposition of carbonates. The decomposition temperature matched the temperature for decomposition of carbonate, with the phase transformation process corresponding to the solid state synthesis of perovskite from 900 $^oC$ to 1200 $^oC$. At this temperature range, the formation of the cubic structure of BCZY can be achieved. When relating the results to the XRD pattern of the sample with perovskite structure after the reversibility treatment, it was proved that the degradation was reversible due to the decomposition of carbonates and the reconstruction of the perovskite structure.

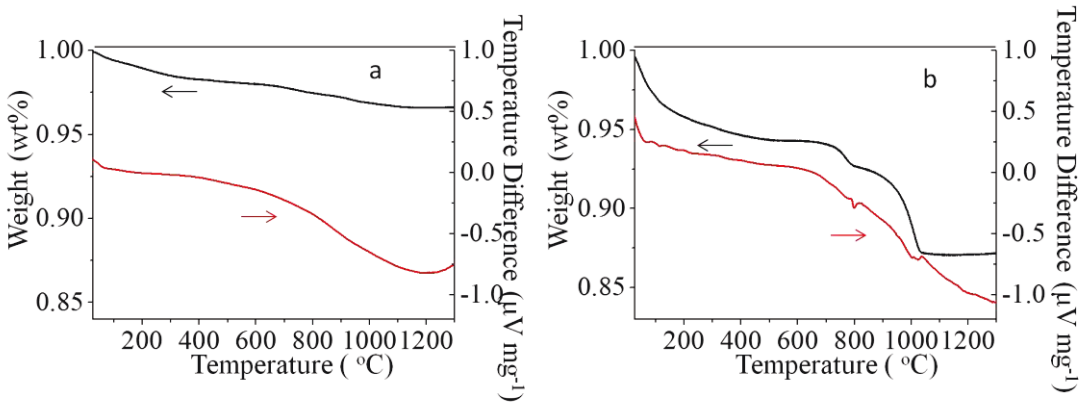


Fig. 4.13. Weight percent \ DTA vs. temperature curves of a. fresh BCZY, and b. degraded BCZY.

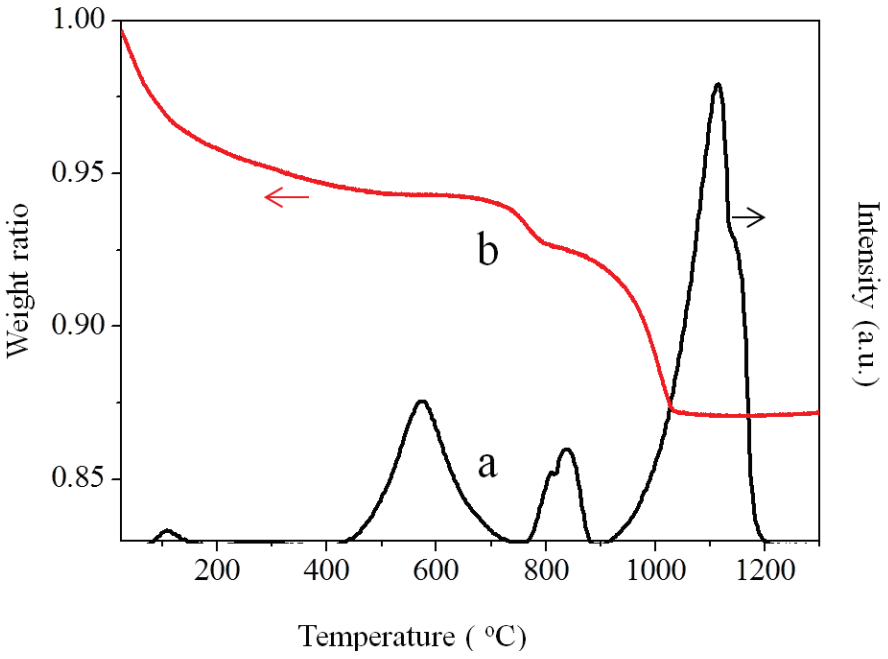


Fig. 4.14. a. Mass spectrum $CO_2$ and b. weight vs. temperature curves for the degraded BCZY.

The mass spectrum of the degraded sample as a function of temperature in Fig. 4.14 confirms the formation of $BaCO_3$ in the degraded BCZY, due to the $CO_2$ emission at above 1000 °C. The equation of the thermal decomposition is as below:

$$BaCO_3 = BaO + CO_2 \quad (4.1)$$

At temperature below 200 °C, the peak of $CO_2$ was referred to the release of $CO_2$ adsorbed on the surface of the sample. The release of $CO_2$ at 600 °C and 800 °C was attributed to the decomposition of other carbonates. It is tentatively suggested that the carbonates were $Y_2O_2CO_3$ and $Y_2(CO_3)_3$, which decomposed at around 800 °C and 600 °C [71] with the equations shown below:

$$Y_2O_2CO_3 = Y_2O_3 + CO_2 \quad (4.2)$$

$$Y_2(CO_3)_3 = Y_2O_3 + 3CO_2 \quad (4.3)$$

### 4.2.6. FT-IR Analysis

The presence of an O-H bond was confirmed in the FT-IR spectrum in Fig. 4.15, suggesting that the adsorption of $H_2O$ on BCZY was inevitable. The wide adsorption bands around 3421 $cm^{-1}$ represented the stretching vibration of the O-H bond [72]. Moreover, other band vibrations were discovered: the strong adsorption bands around 857 $cm^{-1}$ belong to the vibration of $OYCO^{+}$, and several bands at 2449 $cm^{-1}$ ($HCO^{2-}$) , 1450 $cm^{-1}$ ($H_2CO_3^{-}$), 1059 $cm^{-1}$ (HBaOH) were identified as well [72, 73, 74, 75].

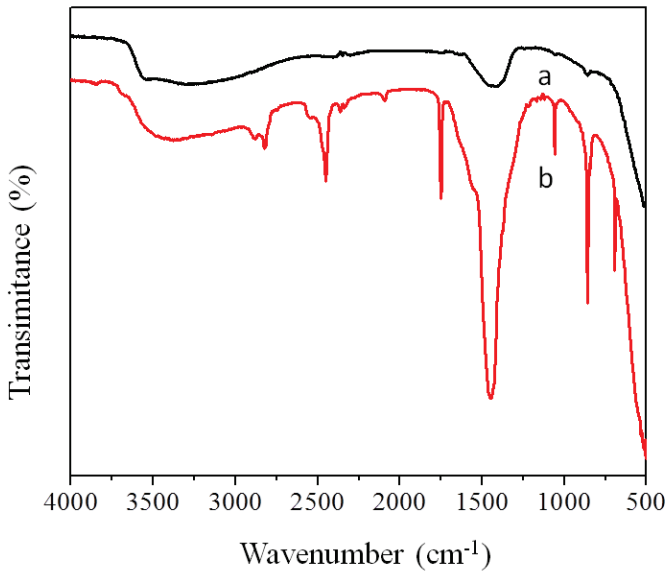


Fig. 4.15. FT-IR spectra of a. the reference specimen, and b. the degraded specimen.

### 4.3 Degradation Mechanisms

Based on the experimental results, low-temperature degradation mechanism of BCZY should occur in the following steps (Fig. 4.16):

(1) The physical and chemical adsorption of $H_2O$ onto the surface of the perovskite-structure electrolyte.

(2) The formation of $OH^{-}$ from $H_2O$ and lattice oxygen on the surface [57].

$$H_2O(g) + O_O^x + v_{\ddot{o}} = 2OH_O \quad (4.4)$$

In the equation, $O_O^x$ refers to the oxygen ions in the cell unit, while $v_{\ddot{o}}$ represents the oxygen vacancy.

(3) The diffusion of $OH^-$ ions (precisely, proton jump mechanism on oxide host ions in the lattice) aggravated at the surface, replacing O in the perovskite structure. $CO_2$ adsorbs and reacts with $OH^-$ connected with Ba, forming $BaCO_3$. The new phases dissolve from the sites of the cubic structure.

Formation of $CeO_2$ and $BaCO_3$ follow Equations (4.5) and (4.6) [76]:

$$BaCeO_3 + H_2O = Ba(OH)_2 + CeO_2 \quad (4.5)$$

$$Ba(OH)_2 + CO_2 = BaCO_3 + H_2O \quad (4.6)$$

The net reaction is :

$$BaCeO_3 + CO_2 = BaCO_3 + CeO_2 \quad (4.7)$$

Initiated by Equation 4.5, the formation of water in Equation 4.6 also accelerates the process.

(4) Cracks originate from grain boundaries. Diffusion of $OH^-$ aggravates further degradation by ruining the inner lattice [77].

(5) In term of electrolyte discs, cracks reduce densification of the discs, aggravating degradation as it creates channel for gas transfer within the lattice of perovskite.

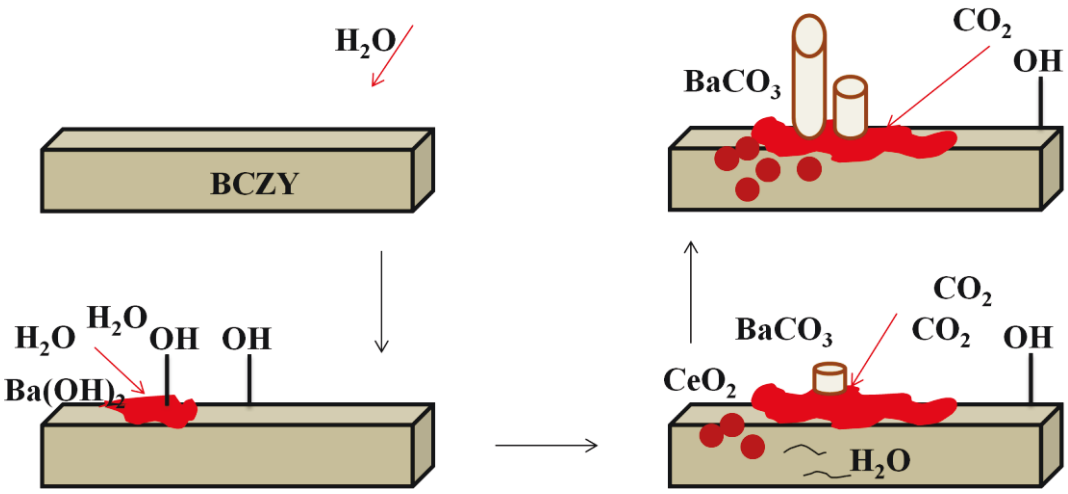


Fig. 4.16. Schematic of the degradation process of BCZY.

The formation of the new phase can be explained as follows: The formation of $BaCO_3$ starts on a two-dimensional flat plane (horizontal) due to the lowest energy needed in formation. The flat growth leads to the crystal growth in the vertical position and results in the rod or cylindrical shape of the new phase [78].

## 4.4 Possible Solutions for Preventing the Degradation of BCZY

Based on the proposed mechanism, several possible solutions to avoid such degradation can be prepared and tested:

### 4.4.1 Composition of Materials

$BaZrO_3$ does not contribute to the degradation of the perovskite structure of BCZY. Improving on the doping ratio of Zr into the mixed site occupancy of Ce is essential to acquire higher stability.

### 4.4.2 Fabrication Methods

The entire fabrication procedure, from the preparation of precursor, co-pressing to sintering, (nano-particle size, thoroughness of the combustion, sintering temperature, pressing pressure, etc.) has a direct effect on the structure and properties of the fabricated samples. Thus, the process needs to be adjusted to avoid the

contamination of certain impurities, to increase grain density and to reduce original micro-cavities, gaps or cracks [79]. These defects may act as the source of crystal structure breakdown or impurities pathway and eventually initiate the performance degradation. Among those methods, densification of discs is the most important approach in providing the less vulnerable BCZY electrolyte disc.

### 4.4.3 Storage Condition

Careless storage is also blamed for the degradation of several previous samples. Fresh sintered samples need to be preserved in a dry environment to eliminate external causes of degradation. It was observed that the fresh BCZY discs, when left in air, degraded and cracked within 20 days, whereas the BCZY discs stored in a dry environment kept their integrity after exposure for the same time frame.

### 4.4.4 Reversibility Treatment

The degraded BCZY discs can be ball milled and then sintered at around 1200 $^{o}$C for 10 hours to decompose residues resulted from the degradation. The process rebuilds the structure of BCZY, as was proved by the reversibility treatment.

# Chapter 5. Conclusions and Future work

The research work in this thesis is categorized into two parts, as described in Chapter 3 and Chapter 4.

## 5.1 LSBT-based Anode Material Prepared by the Impregnation Method

The focus of Chapter 3 was on the development of a SOFC anode catalyst using the infiltration method. The developed anode catalyst was applied on syngas fuelled SOFCs. Conclusions are shown below:

1. Pre-infiltration of $CeO_2$ into LSBT substrate enhanced thermal stability of the dispersed metallic catalysts.
2. $Co/CeO_2$ improved chemical and thermal stabilities than Co/Cu.
3. The fuel cell with 10.5 wt% $CeO_2$ and 2 wt% Co infiltrated LSBT/YSZ anode was electrochemically stable under potentiostatic run for 24 h in syngas.

## 5.2 Degradation of Proton-conducting Material: $BaCe_{0.7}Zr_{0.1}Y_{0.2}O_{3-\delta}$ at Room Temperature

In Chapter 4, the mechanism of the degradation of BCZY, used as electrolyte material for proton conducing SOFCs, was studied. And the results permit the following conclusions:

**1.** Based on the XRD results, the degradation of BCZY was initialized on $BaCeO_3$. At the first stage, $H_2O$ played a crucial role in initializing the degradation by replacing O with $OH^-$, which changed the lattice structure.

**2.** Diffusion of $H_2O$, $CO_2$ and $OH^-$ into the lattice accelerated the process of degradation and resulted in the formation of $BaCO_3$, which grew as segregated cylindrical particles.

**3.** The degradation is reversible.

**4.** Based on the mechanism, several suggestions are given to prevent the degradation:

- Improving the ratio of Zr in the B site enhanced the stability of BCZY.

- Preserving fresh BCZY discs in a dry environment helped to eliminate degradation.

## 5.3 Future Work

It is noted that by changing the ratio of infiltrates, the stability and electrochemical performance of $Co/Cu/CeO_2$ can be further balanced with potential to be applied in other hydrocarbon-fueled systems. It is suggested that the optimization of anode performance can be further studied in direct utilization of methane which is more prone to carbon deposition.

The mechanism of degradation of BCZY suggests that improving the ratio of Zr in B site enhances the stability of BCZY. However, the role that Y played in the degradation at room temperature has not been well understood. Further investigation should be conducted to explore the unknown area.

## References


[1] U.S., Energy Information Administration. International Energy Outlook 2006, June 2006.

[2] Kenney. B., "An Experimental and Modelling Study of Oxygen Reduction in Porous LSM/YSZ Solid Oxide Fuel Cell Cathodes." (2010).

[3] Verrastro. F., Ladislaw. S., Washington Quarterly 30.4 (2007): 95-104.

[4] France., Energy Information Administration. International Energy Outlook 2004, June 2004.

[5] Singhal. S., "High-temperature Solid Oxide Fuel Cells: Fundamentals, Design and Applications: Fundamentals, Design and Applications." (2003).

[6] O'Hayre. R., Cha. S-W., Whitney. C., Fritz. B. P., "Fuel cell fundamentals." (2006).

[7] Sasaki. K., Susuki. K., Iyoshi. A., Uchimura. M., Imamura. N., Kusaba. H., Teraoka. Y., Fuchino. H., Tsujimoto. K., Uchida. Y., Jingo. N., Journal of the Electrochemical Society 153.11 (2006): A2023-A2029.

[8] Tietz. F., Ionics 5.1-2 (1999): 129-139.

[9] Vohs. J. M., Gorte. R. J., Advanced Materials 21.9 (2009): 943-956.

[10] Tsai. T., Barnett. S., Solid State Ionics 93.3 (1997): 207-217.

[11] Seungdoo. P., Vohs. J. M., Gorte. R. J., Nature 404.6775 (2000): 265-267.

[12] Tsoga. A., Naoumidis. A., Nikolopoulos. P., Acta materialia 44.9 (1996): 3679-3692.

[13] Toebes. M. L., Bitter. J. H., Van Dillen. A. J., De Jong. K. P., Catalysis today 76.1 (2002): 33-42.

[14] Kim. T., Liu. G., Boaro. M., Lee. S. I., Vohs. J. M., Gorte. R. J., Al-Madhi. O. H., Dabbousi. B. O., Journal of Power Sources 155.2 (2006): 231-238.

[15] Gross. M. D., Vohs. J. M., Gorte. R. J., Electrochemical and solid-state letters 10.4 (2007): B65-B69.

[16] Au. C. T., Ng. C. F., Liao. M. S., Journal of Catalysis 185.1 (1999): 12-22.

[17] Itome. M., Alan. E. N., Catalysis letters 106.1-2 (2006): 21-27.

[18] Takeguchi. T., Kikuchi. R., Yano. T., Eguchi. K., Catalysis today 84.3 (2003): 217-222.

[19] Vohs. J. M., Gorte. R. J., Electrochemical and Solid-State Letters 8.6 (2005): A279-A280.

[20] Kim. G., Corre. G., Irvine. J. T. S., Vohs. J. M., Gorte. R. J., Electrochemical and solid-state letters 11.2 (2008): B16-B19.

[21] Glazer. A. M., Theoretical and General Crystallography 31.6 (1975): 756-762.

[22] Patil. S., Seal. S., Guo. Y., Schulte. A., Applied physics letters 88.24 (2006): 243110-243110.

[23] Pudmich. G., Boukamp. B. A., Gonzalez-Cuenca. M., Jungen. W., Zipprich. W., Tiets. F., Solid State Ionics 135.1 (2000): 433-438.

[24] Richter. J., Holtappels P., Graule. T., Nakamura. T., Gauckler. L. J., Monatshefte für Chemie-Chemical Monthly 140.9 (2009): 985-999.

[25] Slade. R. C. T., Singh. N., Solid State Ionics 61.1-3 (1993): 111-114.

[26] Iwahara. H., Uchida. H., Ono. K., Ogaki. K., Journal of the Electrochemical Society 135.2 (1988): 529-533.

[27] Uchida. H., Maeda. N., Iwahara. H., Journal of Applied Electrochemistry 12.6 (1982): 645-651.

[28] Bhide. S. V., Virkar. A. V., Journal of the Electrochemical Society 146.6 (1999): 2038-2044.

[29] Matsumoto. H., Kawasaki. Y., Ito N., Enoki. M., Ishihara. T., Electrochemical and Solid-State Letters 10.4 (2007): B77-B80.

[30] Ryu. K. H., Haile. S. M., Solid State Ionics 125.1 (1999): 355-367.

[31] Iwahara. H., Solid State Ionics 61.1 (1993): 65-69.

[32] Zhou. X., Yan. N., Chuang. K. T., Luo. J., RSC Advances 4.1 (2014): 118-131.

[33] Crottaz. O., Kubel. F., Schmid. H., Journal of Solid State Chemistry 122.1 (1996): 247-250.

[34] Leng, Y., “Material Characterizations” (2013).

[35] Atkinson. A., Barnett. S., Gorte. R. J., Irvine. J. T. S., McEvoy. A. J., Mogensen. M., Singhal. S. C., Vohs. J. M., Nature materials 3.1 (2004): 17-27.

[36] Liu. J., Barnett. S., Solid State Ionics 158.1 (2003): 11-16.

[37] Stambouli. A. B., Traversa. E., Renewable and Sustainable Energy Reviews 6.5 (2002): 433-455.

[38] Yan. N., Fu. X., Chuang. K. T., Luo. J., Journal of Power Sources 254 (2014): 48-54.

[39] Kharton. V. V., Marques. F. M. B., Current Opinion in Solid State and Materials Science 6.3 (2002): 261-269.

[40] Sholklapper. T. Z., Kurokawa. H., Jacobson. C. P., Visco. S. J., De Jonghe. L. C., nano letters 7.7 (2007): 2136-2141.

[41] Sun. X., Wang. S., Wang. Z., Ye. X., Wen. T., Huang. F., Journal of Power Sources 183.1 (2008): 114-117.

[42] Pillai. M. R., Kim. I., Bierschenk. D. M., Barnett. S. A., Journal of Power Sources 185.2 (2008): 1086-1093.

[43] Marina. O. A., Canfield. N. L., Stevenson. J. W., Solid State Ionics 149.1 (2002): 21-28.

[44] Vincent. A. L., Hanifi. A. R., Luo. J., Sanger. A. R., Journal of Power Sources 195.3 (2010): 769-774.

[45] Vincent. A. L., Hanifi. A. R., Luo. J., Chuang. K. T., Sanger. A. R., Etsell. T. H., Sarkar. P., Journal of Power Sources 215 (2012): 301-306.

[46] Adijanto. L., Bennett. D. A., Chen. C., Yu. A. S., Cargnello. M., Fornasiero. P., Gorte. R. J., Vohs. J. M., Nano letters 13.5 (2013): 2252-2257.

[47] Gross. M. D., Vohs. J. M., Gorte. R. J., Electrochimica acta 52.5 (2007): 1951-1957.

[48] Lee. S. I., Vohs. J. M., Gorte. R. J., Journal of the Electrochemical Society 151.9 (2004): A1319-A1323.

[49] Jiang. S-P., Yvonne. D. Y., Jonathan. G. L., Journal of the E lectrochemical Society 149.9 (2002): A1175-A1183.

[50] Jiang. S. P., Materials Science and Engineering: A 418.1 (2006): 199-210.

[51] Weber. A., Sauer B., Müller. A. C., Herbstritt. D., Ivers-Tiffee. E., Solid State Ionics 152 (2002): 543-550.

[52] Klemensø. T., Thydén. K., Chen. M., Wang. H. J., Journal of Power Sources 195.21 (2010): 7295-7301.

[53] Costa-Nunes. O., Gorte. R. J., Vohs. J. M., Journal of Power Sources 141.2 (2005): 241-249.

[54] Kan. H., Lee. H., Applied Catalysis B: Environmental 97.1 (2010): 108-114.

[55]Lei. Z., Zhu. Q., Han. F., Acta Physico-Chimica Sinica 3 (2010): 013.

[56] Di Bartolomeo. E., D'Epifanio. A., Pugnalini. C., Zunic. M., D'Ottavi. C., Licoccia. S., ECS Transactions, 28.11 (2010): 259-265.

[57] Fabbri. E., Bi. L., Pergolesi. D., Traversa. E., Advanced Materials 24.2 (2012): 195-208.

[58] Kreuer. K. D., Annual Review of Materials Research 33.1 (2003): 333-359.

[59] Kreuer. K. D., Chemistry of Materials 8.3 (1996): 610-641.

[60] Fabbri. E., D'Epifanio. A., Di Bartolomeo. E., Licoccia. S., Traversa. E., Solid State Ionics 179.15 (2008): 558-564.

[61] Zuo. C., Zha. S., Liu. M., Hatano. M., Uchiyama. M., Advanced Materials 18.24 (2006): 3318-3320.

[62] Christie. A. B., Lee. J., Sutherland. I., Walls. J. M., Applications of surface science 15.1 (1983): 224-237.

[63] Clinton. J. C., "Colloidal Cerium Oxide Nanoparticle: Synthesis and Characterization Techniques." (2008).

[64] Paparazzo. E., Ingo. G., M. Zacchetti. N., Sci. Technol. A9, 1416 (1991): 1306-38-3

[65] Moulder. J. F., Stickle. W. F., Sobol. P. E., Bomben. K. D., "Handbook of X-ray photoelectron spectroscopy. Eden Prairie, Minnesota: Physical Electronics." (1995).

[66] Ingo. G.M., Paparazzo. E., Bagnarelli. O., Zacchetti. N., Surf. Interface Anal. 16, 515 (1990):515-519

[67] Reichl. R., Gaukler. K. H., Applied Surface Science 26.2 (1986): 196-210.

[68] Ricote. S., Nikolaos. B., Caboche. G., Solid State Ionics 180.14 (2009): 990-997.

[69] Bouwmeester. H. J. M., Kruidhof. H., Burggraaf. A. J., Solid State Ionics 63 (1993): 816-822.

[70] Haile. S. M., Staneff. G., Ryu. K. H., Journal of Materials Science 36.5 (2001): 1149-1160.

[71] Matsushita. N., Tsuchiya. N., Nakatsuka. K., Yanagitani. T., Journal of the American Ceramic Society 82.8 (1999): 1977-1984.

[72] Trezza. M. A., Lavat. A. E., Cement and Concrete Research 31.6 (2001): 869-872.

[73] Zhou. M,, Andrews. L., Journal of the American Chemical Society, 1998, 120(44): 11499-11503.

[74] Jacox. M. E., Journal of Physical and Chemical Reference Data, 1998, 27(2): 115-393.

[75] Kauffman. J. W., Hauge. R. H., Margrave. J. L., High temperature science, 1984, 18(2): 97-118.

[76] Tanner. C. W., Fung. K. Z., Virkar. A. V., Journal of The Electrochemical Society 143.4 (1996): 1386-1389.

[77] Kreuer. K. D., Solid State Ionics 125.1 (1999): 285-302.

[78] Boston. R., Schnepp. Z., Nemoto. Y., Sakka. Y., Hall. S. R., Science 344.6184 (2014): 623-626.

[79] Sawant. P., Varma. S., Wani. B. N., Bharadwaj. S. R., International Journal of Hydrogen Energy 37.4 (2012): 3848-3856.